

Multi-Stability Property of Magneto-Kresling Truss Structures

Xinyan Yang

Department of Civil and Environmental Engineering,
Northwestern University,
2145 Sheridan Road,
Evanston, IL 60208
e-mail: xinyanyang2024@u.northwestern.edu

Sinan Ketten¹

Mem. ASME
Department of Civil and Environmental Engineering,
Department of Mechanical Engineering,
Northwestern University,
2145 Sheridan Road,
Evanston, IL 60208
e-mail: s-ketten@northwestern.edu

The Kresling truss structure, derived from Kresling origami, has been widely studied for its bi-stability and various other properties that are useful for diverse engineering applications. The stable states of Kresling trusses are governed by their geometry and elastic response, which involves a limited design space that has been well explored in previous studies. In this work, we present a magneto-Kresling truss design that involves embedding nodal magnets in the structure, which results in a more complex energy landscape, and consequently, greater tunability under mechanical deformation. We explore this energy landscape first along the zero-torque folding path and then release the restraint on the path to explore the complete two-degree-of-freedom behavior for various structural geometries and magnet strengths. We show that the magnetic interaction could alter the potential energy landscape by either changing the stable configuration, adjusting the energy well depth, or both. Energy wells with different minima endow this magneto-elastic structure with an outstanding energy storage capacity. More interestingly, proper design of the magneto-Kresling truss system yields a tri-stable structure, which is not possible in the absence of magnets. We also demonstrate various loading paths that can induce desired conformational changes of the structure. The proposed magneto-Kresling truss design sets the stage for fabricating tunable, scalable magneto-elastic multi-stable systems that can be easily utilized for applications in energy harvesting, storage, vibration control, as well as active structures with shape-shifting capability. [DOI: 10.1115/1.4051705]

Keywords: origami, multi-stable structure, magneto-active structure, magneto-elastic coupling, energy storage

1 Introduction

Origami is a well-known ancient art of paper folding. Common origami expressions include Yoshimura pattern, Kresling pattern, Miura-ori pattern, and waterbomb base [1]. Apart from its esthetic value, origami has been foundational for engineering folded structures that broke new ground in applications including medical equipment [2–4], ballistic shields [5], and aerospace devices [6–8]. While traditional origami involves folding sheets, origami units or building blocks can also be tessellated into multidimensional lattices, forming so-called origami-inspired metamaterials [9–14], displaying controllable mechanical properties, like the tunable thermal expansion [15] and adjustable Poisson's ratio [16].

General multi-stable structures possess several energy wells, thus various stable states. Statically, under external mechanical perturbations, the system may shift from one stable state to another along with shape and energy changes. Dynamic excitations with sufficient amplitude can result in transitions from linear or weakly nonlinear intra-well fluctuations to highly nonlinear inter-well oscillations of the system [17]. These features make the multi-stable structure an ideal platform for applications like energy adsorption [18–20], energy harvesting [20–23], vibration control [24–28], and mechanical switches [29,30]. Investigating the number and position of the existing stable states is necessary for designing systems that suit these purposes. Remarkably, many origami structures have more than a single stable state. The Kresling pattern has been studied extensively due to its ability to undergo both vertical and rotational deformations in the deployment. The 2D crease pattern and the folded 3D cylindrical model for a typical Kresling origami are

shown in Figs. 1(a) and 1(b), respectively. The initial configuration dictates the number of stable states that the structure will have. This has been explored previously either using a Kresling origami with six elements [31] or a simplified origami-inspired pentagon-based Kresling truss model [29]. In the truss model, the original Kresling origami panels are removed and creases are replaced with elastic truss members connecting vertices of top and bottom rigid regular polygons, as shown in Fig. 1(c) with detailed description in Sec. 2. Compared with the Kresling origami cylinder, the truss model simplifies the analysis by changing the system potential energy contributions from non-rigid panel deformation to elastic truss elongation. This simplification also generalizes this specific origami structure to a network system with only nodal interactions, which may help with finding its analogies in other fields, like biological systems where elastic network models are prevalently used for describing mechanical phenomena [32–34]. Further investigation of this truss representation and its multi-stability property illustrates the relationship between the rich motion paths [35] and some instability-induced phenomena, like bifurcation, snapback, and reverse rotation [36].

A shortcoming of the purely elastic Kresling truss structure is that it can display at most two potential energy minima with zero-strain energies; thus, it is unable to store or release energy due to conformational changes. To solve this problem, we get inspired by magneto-active soft materials made up of elastomers with embedded magnetic particles and cured with controlled magnetic fields [37,38]. These magneto-active soft materials exhibit tunable mechanical properties and shape-shifting ability, and have been exploited in designs for applications ranging from damping systems [39–42] to soft actuators [43–47]. In addition, some magneto-elastic mechanical metamaterials have been prospected for energy dissipation and wave filtering by incorporating discrete permanent magnets and periodic elastic lattices [48–50]. Based on these findings, we hypothesized that introducing nodal magnets to

¹Corresponding author.

Contributed by the Applied Mechanics Division of ASME for publication in the JOURNAL OF APPLIED MECHANICS. Manuscript received May 9, 2021; final manuscript received July 5, 2021; published online July 29, 2021. Tech. Editor: Yonggang Huang.

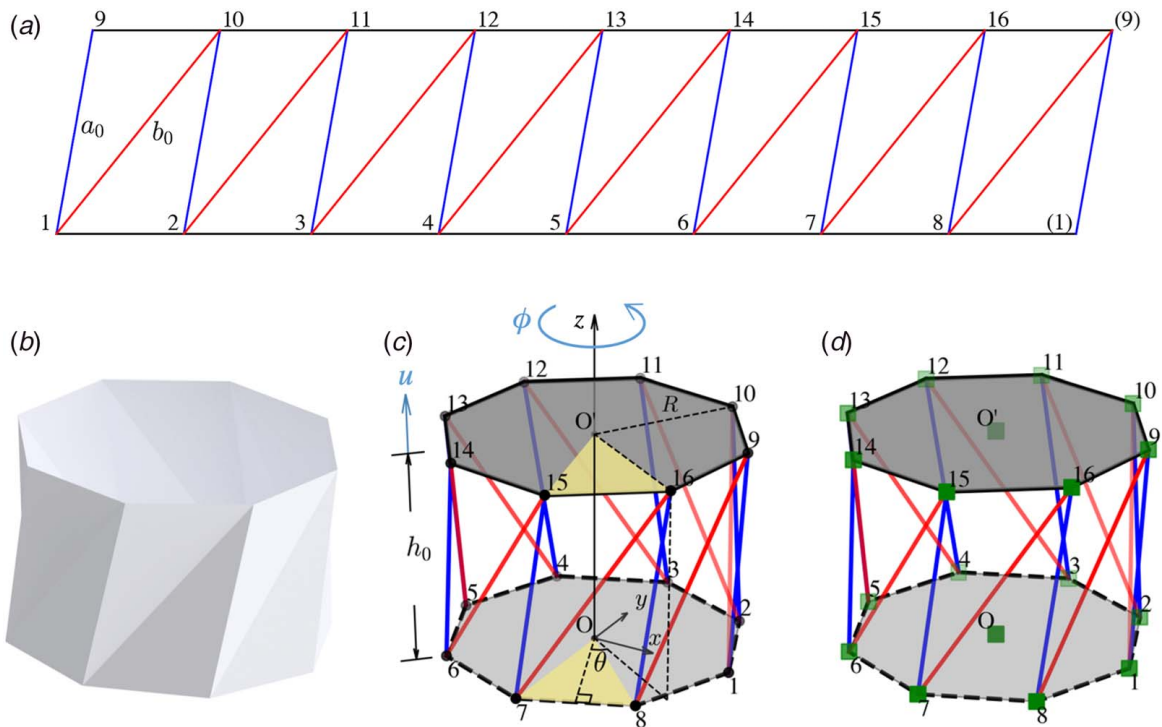


Fig. 1 (a) The crease pattern, (b) Kresling origami cylinder, (c) Kresling truss structure with the initial configuration $(h_0, \theta_0) = (110 \text{ mm}, 35 \text{ deg})$, $R = 90 \text{ mm}$, and $n = 8$ (octagon-based), (d) Magneto-Kresling truss structure with possible magnet embedding sites shown as solid squares (Color version online.)

the Kresling truss structure to generate noncontact, nonlinear magnetic interactions superposed with elastic contributions could alter energy landscapes that could result in three or more stable states. Indeed, systems with complementary dipole interactions (electrostatic instead of magnetostatic) are commonly found in structural protein motifs that exhibit outstanding mechanical properties such as energy dissipation and storage capacity [51,52]. We show in Fig. 1(d) that the Kresling truss model is a good candidate for a tunable magneto-elastic system because it offers easily accessible magnet mounting sites marked by solid squares. Embedding permanent magnets in an origami structure to change its stability profile was first reported by Fang et al. using the stacked Miura-ori structure and the Kresling origami [53]. They showed that embedding magnets in a bi-stable Kresling origami could shift the two stable states in the folding process and bring the magneto-origami structure to another stable state at zero height. Their experiments validated the quantitative change of the stable states at relatively large structural heights but huge discrepancies occurred in the low-height region where the strong magnetic interactions prohibited further development of rotation angle along the desired deformation path and compressed the origami facet material substantially. In the magneto-Kresling structure we proposed here, via replacing thin-walled origami panels with the truss system, the kinematic constraints from allowable elastic deformations of the panel on restraining the coupling between the vertical displacement and rotation angle are released such that we could take into account both the magnetic interactions and elastic potentials in determining the coupling behavior along the path.

In this study, the bi-stability property of Kresling truss systems without magnets is first briefly illustrated, followed by a detailed discussion on the magneto-elastic coupling effect observed in the multi-stable magneto-Kresling truss structure. Our numerical study reveals that the magnetic interaction not only enables prescribing the number of stable states and shifting the potential energy well positions while controlling well depths but also influences the kinematics along the folding path. We show several possible quasi-static loading paths joining different stable states, which

can be traversed either by displacement-controlled deformation with free rotation, rotation-controlled deformation with free vertical displacement, or a combination of both. Prior works have mostly set the external torque to zero in the deployment and ignored other paths [29,30], because both of the local minima for a purely elastic bi-stable Kresling truss structure could be visited along such a zero-torque path. Nevertheless, we show that the magneto-Kresling truss system subjected to an external torque may reach a local potential energy minimum which is inaccessible under loading with only axial compression or tension. This potential energy minimum with trusses locked in a relatively heavily stretched configuration plays an important role in gaining a high-energy storage capacity. Finally, we demonstrate the dependence of the number of stable states and energy storage capacity on several design parameters. The path-dependent multi-stability property and the highly tunable potential energy landscape intrinsic to the magneto-Kresling truss structure are expected to advance the design and engineering of origami-inspired multi-stable metamaterials.

2 Methods

2.1 Elastic Force and Potential.

The Kresling truss unit has two identical rigid regular polygons with n vertices/edges with a circumscribed circle of radius R . The two polygons share the same out-of-plane rotation axis and are separated by a center-to-center distance h_0 along this axis, which is the initial height of the structure. The polygons are connected by elastic trusses and offset by a relative rotation angle θ , defined as the angle between the perpendicular bisector of a bottom polygon edge in an isosceles triangle and the projection of the right edge of its counterpart triangle (the one connected by the same mountain creases) in the top polygon. This definition simplifies the calculation mathematically [29]. Initially, the relative angle is θ_0 and lengths for mountain and valley trusses are a_0 and b_0 , respectively. A schematic of the structure is shown in Fig. 1(c). In our analysis,

we only consider counter-clockwise θ_0 since the derivation of the clockwise case is similar. The bottom polygon is held fixed and cannot be displaced or rotated. Under a vertical force and/or torque applied on the top polygon, the Kresling truss structure folds (contracts) or unfolds (expands) with two degrees-of-freedom (DOF) globally, i.e., vertical displacement, u , along the z -axis, and rotation angle, $\varphi = \theta - \theta_0$, about the z -axis. Upward displacement and anti-clockwise rotation angle are positive by convention. The structure reaches its maximum or minimum rotation angle when all the valley or mountain creases intersect at the same point, resulting in $\varphi_{\max} = (\pi - \pi/n) - \theta_0$ and $\varphi_{\min} = -[(\pi - \pi/n) + \theta_0]$, respectively. Additionally, to prevent close contact between top and bottom polygons (steric clash of structural elements), the minimum vertical displacement is set to $-0.8h_0$ in this study.

Nodal forces acting in x , y , and z directions in response to truss elongation at structural deformation (u , φ) can be evaluated by structural matrix analysis [54]. Consider a system with $2N$ nodes (first N nodes from the bottom polygon and another N nodes from the top) and V trusses (here $V = 2N$). Nodal forces are represented by a $6N \times 1$ force matrix \mathbf{P} :

$$\mathbf{P} = \mathbf{B}\mathbf{Q}_f \quad (1)$$

where

$$\mathbf{P} = [F_{1,x} \ F_{1,y} \ F_{1,z} \ F_{2,x} \ F_{2,y} \ F_{2,z} \ \cdots \ F_{2N,x} \ F_{2N,y} \ F_{2N,z}]^T$$

\mathbf{Q}_f is a $V \times 1$ element force matrix:

$$\mathbf{Q}_f = [q_1 \ q_2 \ \cdots \ q_v \ \cdots \ q_V]^T, \quad q_v = k_v \cdot (l_v - l_{v0})$$

The v th entry, q_v , stands for the axial force of the v th truss, with initial length l_{v0} and stiffness k_v . l_v is the truss length when the system undergoes deformation (u , φ). The geometry, end forces, and element force of truss v are depicted in the left panel of Fig. 2. \mathbf{B} is a $6N \times V$ structure strain–displacement matrix, which can be calculated from the summation of element strain–displacement matrix \mathbf{B}_v . For the v th truss connecting node i

and j ,

$$\mathbf{b}_v = \begin{bmatrix} b_{v,1} \\ b_{v,2} \\ b_{v,3} \\ b_{v,4} \\ b_{v,5} \\ b_{v,6} \end{bmatrix} = \begin{bmatrix} -\frac{X_j - X_i}{l_v} \\ \frac{Y_j - Y_i}{l_v} \\ -\frac{Z_j - Z_i}{l_v} \\ \frac{X_j - X_i}{l_v} \\ \frac{Y_j - Y_i}{l_v} \\ \frac{Z_j - Z_i}{l_v} \end{bmatrix},$$

$$\mathbf{B}_v = \begin{bmatrix} 1 & 2 & \cdots & v-1 & v & v+1 & \cdots & V \\ 0 & 0 & \cdots & 0 & 0 & 0 & \cdots & 0 \\ \vdots & \vdots & \ddots & \vdots & \vdots & \vdots & \ddots & \vdots \\ 0 & 0 & \cdots & 0 & 0 & 0 & \cdots & 0 \\ 0 & 0 & \cdots & 0 & b_{v,1} & 0 & \cdots & 0 \\ 0 & 0 & \cdots & 0 & b_{v,2} & 0 & \cdots & 0 \\ 0 & 0 & \cdots & 0 & b_{v,3} & 0 & \cdots & 0 \\ 0 & 0 & \cdots & 0 & 0 & 0 & \cdots & 0 \\ \vdots & \vdots & \ddots & \vdots & \vdots & \vdots & \ddots & \vdots \\ 0 & 0 & \cdots & 0 & 0 & 0 & \cdots & 0 \\ 0 & 0 & \cdots & 0 & b_{v,4} & 0 & \cdots & 0 \\ 0 & 0 & \cdots & 0 & b_{v,5} & 0 & \cdots & 0 \\ 0 & 0 & \cdots & 0 & b_{v,6} & 0 & \cdots & 0 \\ 0 & 0 & \cdots & 0 & 0 & 0 & \cdots & 0 \\ \vdots & \vdots & \ddots & \vdots & \vdots & \vdots & \ddots & \vdots \\ 0 & 0 & \cdots & 0 & 0 & 0 & \cdots & 0 \end{bmatrix}_{6N}, \quad \mathbf{B} = \sum_{v=1}^V \mathbf{B}_v$$

In the folding process, nodal position matrix \mathbf{U}_f first gets updated with respect to current vertical displacement u and rotation angle φ using Eq. (2).

$$\mathbf{U}_f = (\mathbf{U}_0 + \Delta\mathbf{U})\mathbf{R} \quad (2)$$

where $\Delta\mathbf{U}$ is the $2N \times 3$ displacement matrix and \mathbf{R} is the 3×3 rotation matrix:

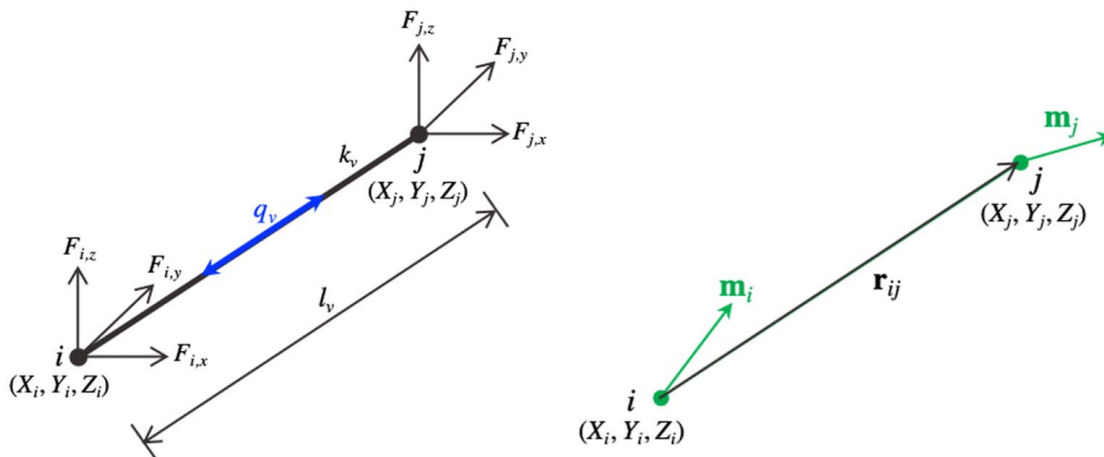


Fig. 2 Left: geometry, end forces, and element force q_v of the v th truss with stiffness k_v and length l_v joining nodes i and j in structural matrix analysis. Right: model for calculating the magnetic force felt by magnetic dipole \mathbf{m}_i from magnetic dipole \mathbf{m}_j . \mathbf{r}_{ij} is the vector from the position of \mathbf{m}_i to \mathbf{m}_j .

$$\Delta \mathbf{U}^T = \begin{bmatrix} 1 & 2 & \dots & N & N+1 & N+2 & \dots & 2N-1 & 2N \\ 0 & 0 & \dots & 0 & 0 & 0 & \dots & 0 & 0 \\ 0 & 0 & \dots & 0 & 0 & 0 & \dots & 0 & 0 \\ 0 & 0 & \dots & 0 & u & u & \dots & u & u \end{bmatrix}$$

$$\mathbf{R} = \begin{bmatrix} \cos \varphi & -\sin \varphi & 0 \\ \sin \varphi & \cos \varphi & 0 \\ 0 & 0 & 1 \end{bmatrix}$$

Then each truss length l_v , structure strain–displacement matrix \mathbf{B} , and element force matrix \mathbf{Q}_e are updated accordingly. Finally, the nodal force matrix \mathbf{P} is obtained. By calculating the resultant force and torque for nodes in the top polygon from \mathbf{P} , we could get force $F_{z,el}$ and torque $T_{z,el}$ acting on the system in response to deformation (u, φ) . We assume all the mountain and valley trusses have the same stiffness k . The elastic potential energy of the system is:

$$E_{el} = \sum_{v=1}^V \frac{1}{2} k (l_v - l_{v,0})^2 \quad (3)$$

For the displacement-controlled zero-torque quasi-static loading path, u changes linearly from the initial value to the target value. Given any u_i in the path, we can find φ_i by imposing $T_{z,el}(u_i, \varphi) = 0$. Similarly, solving $F_{z,el}(u, \varphi_i) = 0$ gives us the displacement u_i for a desired φ_i in the rotation-controlled zero-compression loading path.

This matrix analysis method keeps track of nodal positions in the deployment, which makes later evaluation of magnetic interactions using matrix multiplications based on magnet positions straightforward. It is also applicable to a system with different member stiffnesses. In addition, by simply modifying the nodal position updating rules, i.e., Eq. (2), this model can be extended to a 6-DOF (three translations plus three Euler rotation angles) Kresling truss system, taking both the axial and off-axis responses into consideration [55]. However, this is beyond the scope of our work and left for future studies.

2.2 Magnetic Force and Potential. We assume that magnets discussed here are uniformly magnetized and can be simplified as magnetic point dipoles. This assumption holds if the magnets are small enough or sufficiently distant [56]. Under the point dipole approximation, the magnetostatic energy $e_{mag,ij}$ and force $\mathbf{f}_{mag,ij}$ felt by magnetic dipole \mathbf{m}_i from magnetic dipole \mathbf{m}_j are described by Eqs. (4) and (5), respectively [57–59].

$$e_{mag,ij} = \frac{\mu_0}{4\pi} \left[\frac{(\mathbf{m}_i \cdot \mathbf{m}_j)}{r_{ij}^3} - 3 \frac{(\mathbf{m}_i \cdot \mathbf{r}_{ij})(\mathbf{m}_j \cdot \mathbf{r}_{ij})}{r_{ij}^5} \right] \quad (4)$$

$$\mathbf{f}_{mag,ij} = -\frac{3\mu_0}{4\pi r_{ij}^5} \left[(\mathbf{m}_i \cdot \mathbf{r}_{ij})\mathbf{m}_j + (\mathbf{m}_j \cdot \mathbf{r}_{ij})\mathbf{m}_i + (\mathbf{m}_i \cdot \mathbf{m}_j)\mathbf{r}_{ij} - 5 \frac{(\mathbf{m}_i \cdot \mathbf{r}_{ij})(\mathbf{m}_j \cdot \mathbf{r}_{ij})}{r_{ij}^2} \mathbf{r}_{ij} \right] \quad (5)$$

where \mathbf{r}_{ij} is the vector from node i to node j , and magnitude $r_{ij} = |\mathbf{r}_{ij}|$. Figure 2, right panel, shows the model for calculating the energy and force between two magnets with arbitrary directions of magnetic dipole moments.

For uniformly magnetized permanent magnets, the magnitude of dipole moment $m = |\mathbf{m}| = M \text{Vol}$. Vol is the bar magnet volume. M is saturation magnetization (in A/m) converted from material residual induction B_r (in T), $M = B_r / \mu_0$. B_r is specified by the manufacturer for a given magnet. μ_0 is the permeability of vacuum, $\mu_0 = 4\pi \times 10^{-7}$ H/m. We only consider the case where all magnets embedded in the magneto-Kresling truss structure are of the same size, shape, and strength. We use m^2 (in $\text{A}^2 \text{m}^4$) as the parameter to regulate the magnet strength. Since the elastic energy and magnetostatic energy are proportional to k and m^2 , respectively, the relative strength of the truss and magnet, k/m^2 , plays an important role in tuning the potential energy profile of the truss-and-magnet system.

As mentioned in Sec. 1, magnets can be embedded at different sites with various dipole layouts. To keep the model simple, instead of having magnetic dipoles with arbitrary directions, we only consider those along the rotation axis (z -axis). For the magnet embedment, we could center magnets at top and bottom polygons with purely attractive or repulsive interactions as shown in Figs. 3(a) and 3(b), respectively. If magnets are involved in this way, the magnetostatic energy is governed by the vertical displacement u and is insensitive to the rotation angle φ . Alternatively, magnets could be embedded using a node-centered pattern. For this pattern, in order to avoid uneven forces along z -axis felt by nodal magnets embedded in the same layer and non-trivial resultant forces in and torques about x - and y -axis on the rigid plate, the arrangement of dipole moment directions should either take a layout with n -fold radial symmetry (consistent dipole directions for magnets embedded in the same plate) or an alternate layout (opposite dipole directions for neighboring magnets). Otherwise, without extra constraints, the top plate will slide in the plane perpendicular to z -axis and rotate about x - and y -axis. Again, these motions could be captured by an extended 6-DOF model which is not covered here. In this study, truss-and-magnet systems are all designed using an alternate layout of nodal magnetic dipoles to reach a more variant energy landscape. Figure 3(c) illustrates this layout using an octagon-based magneto-Kresling truss structure. Magnets centered at nodes 1, 3, 5, 7 on the bottom polygon and 10, 12, 14, 16 on the top have the same dipole moment along the $[0, 0, 1]$ direction, while at nodes 2, 4, 6, 8 and 9, 11, 13, 15, magnetic dipoles are along the $[0, 0, -1]$ direction. These alternately

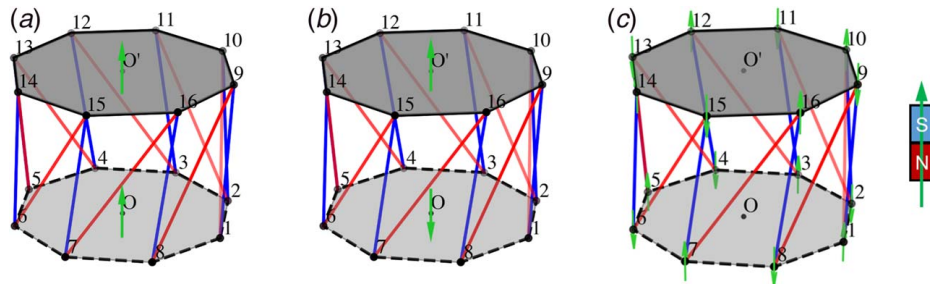


Fig. 3 Typical ways to embed magnets in Kresling truss structures. Magnets are centered at top and bottom polygons with (a) attractive, (b) repulsive interactions, and (c) A magneto-Kresling truss structure with neighboring nodal magnetic dipoles pointing to opposite directions. Arrow depicts point dipole moment direction from north pole to south pole as shown on the right.

arranged dipole moments also break the rotational symmetry for Kresling truss structures with $\theta_0 = 0$. Structures with three other allowable layouts of nodal magnetic dipoles are discussed (in the [Supplemental Material](#) on the ASME Digital Collection), including a different alternate layout with dipoles in the top layer flipped, an attractive layout, and a repulsive layout.

Note that relative positions of magnets on the same layer are fixed in the deployment, leading to in-plane magnetic interactions invariant to vertical displacement u and rotation angle φ . Therefore, only the dipole–dipole energies for inter-layer magnet pairs are considered. Intra-layer dipole–dipole interactions are neglected. If there are N magnets embedded in the bottom and another N in the top, the total magnetostatic energy of the system is

$$E_{\text{mag}} = \sum_{i=N+1}^{2N} \sum_{j=1}^N e_{\text{mag},ij} \quad (6)$$

The magnetic force on node w is

$$\mathbf{F}_{\text{mag},w} \begin{cases} \sum_{i=1+N}^{2N} \mathbf{f}_{\text{mag},wi}, & w = 1, 2, \dots, N \\ \sum_{i=1}^N \mathbf{f}_{\text{mag},wi}, & w = N + 1, N + 2, \dots, 2N \end{cases} \quad (7)$$

By calculating the negative of the resultant force and torque felt by magnets embedded in the top polygon along z -axis (the rotation axis), we could get the input force $F_{z,\text{mag}}$ and torque $T_{z,\text{mag}}$ under any deformation (u, φ) . Combining the truss elastic energy and magnetostatic energy, the total potential energy of the system $E_{\text{tot}}(u, \varphi) = E_{\text{el}}(u, \varphi) + E_{\text{mag}}(u, \varphi)$. The total force $F_z(u, \varphi) = F_{z,\text{el}}(u, \varphi) + F_{z,\text{mag}}(u, \varphi)$ and torque $T_z(u, \varphi) = T_{z,\text{el}}(u, \varphi) + T_{z,\text{mag}}(u, \varphi)$.

2.3 Numerical Search for Local Minimum Energy States.

In most published studies of Kresling origami/truss structures, deployment is assumed to follow a displacement-controlled loading path, where the zero-torque condition restricts the way vertical displacement u and rotation angle φ get coupled, i.e., φ is a known function of u . In this case, the Kresling origami/truss in fact exhibits a pseudo 1-DOF mechanism. The local minima of the potential energy can be found by inspecting the 1D energy curve as a function of u . This pseudo 1-DOF mechanism is the nature of Kresling origami, the predecessor of Kresling truss structure, due to the geometry constraint from the triangular facet. This geometry constraint could be modeled as either the non-deformable mountain [26] or valley [53] creases, based on which φ is calculated for a given value of u . But for the 2-DOF Kresling truss system, this constraint is released, making the structure able to deform along various paths where u and φ are coupled differently. For example, we can force a Kresling truss structure to shift from its first stable configuration to the second by simply compressing it ($F_z \neq 0, T_z = 0$), or compressing and rotating it simultaneously ($F_z \neq 0, T_z \neq 0$), or even just rotating it ($F_z = 0, T_z \neq 0$). Therefore, the 1-DOF solution may miss the energy minima that are not on the presumed zero-torque deployment path for the magneto-Kresling truss structure. A more general approach is to apply the first- and second-order conditions for local minima by finding points (u_s, φ_s) giving zero-force $F_z(u_s, \varphi_s)$ and zero-torque $T_z(u_s, \varphi_s)$ on the convex surface of the 2D energy landscape $E(u, \varphi)$ [36]. The 2D potential energy landscape of the magneto-Kresling truss system is highly nonlinear and complex. Thus, finding analytical solutions by symbolic calculation is challenging. Here, we numerically search stable states (u_s, φ_s) satisfying the first- and second-order conditions for local minima. We first perform a uniform mesh of the accessible (u, φ) space (the upper bound for u is safely set to $0.8h_0$). Starting from each grid point (u_i, φ_j) , “hybr” solver in `scipy.optimize.root` package [60] is used to find the root for functions $F_z(u, \varphi)$ and $T_z(u, \varphi)$. Then, for points found by the solver, we remove those not in the domain of

our interest, such as roots with $u < -0.8h_0$, and those giving negative eigenvalues of the Hessian matrix, which violate the second-order condition. For a given structure, its stable states found by this search algorithm depend on the mesh of the accessible deformation space. A coarse mesh with large spacing in either u or φ may lead to the missing of local minima which could only be reached by the solver from starting points between two grid points. Thus, we iteratively perform this numerical search protocol until the detected stable states do not change with the mesh of (u, φ) space. The mesh goes from 20×20 to 30×30 , 40×40 , and so on, with 30×30 being sufficient for all of our cases reported herein.

3 Results

3.1 Truss-Only System

3.1.1 Multi-Stability Property of Octagon-Based Kresling Truss Structures. In this section, we briefly discuss the multi-stability property of octagon-based ($n = 8$) Kresling truss structures without magnets. The model displays either mono-stable state or bi-stable states in the deployment, dependent on its initial equilibrium configuration characterized by height-to-radius ratio h_0/R and initial rotation angle θ_0 . A mono-stable Kresling truss structure can only rest at its initial state $S_0(u, \varphi) = (0, 0)$. For the bi-stable case, the first stable state S_0 is the initial configuration $(0, 0)$, while the second minimum energy position S_1 can either appear in the contracted shape ($u < 0, \varphi > 0$) or in the expanded shape ($u > 0, \varphi < 0$), as illustrated in Figs. 4(a) and 4(b), respectively. The potential energy minima are denoted by the white crosses in the energy landscape. The vertical displacement u and potential energy E are normalized by structure initial height h_0 and energy kh_0^2 , respectively. It is notable that the potential energy minima for Kresling truss structures arise at zero-strain configurations, where all of the linear elastic truss members are at their initial lengths. These zero-strain positions are determined only by the geometry and are insensitive to the truss stiffness. The net expended energy in the conformational change is zero.

3.1.2 Effect of Different Polygon Shapes. In order to investigate how the multi-stability property would depend on shape of the regular polygon, as determined by the number of vertices, n , we examined systems with n ranging from 4 to 10. We only consider polygons with even numbers of vertices because they offer magnet embedding sites compatible with the nodal magnet layout as described in Fig. 3(c), which is used in the later discussion of magneto-Kresling truss structures. For each n , we search potential energy minima in the constrained (u, φ) domain for structures with different initial configurations. In the multi-stability diagram shown in Fig. 5, structures with different combinations of $(h_0/R, \theta_0)$ are labeled using numbers of stable states they have. As in previous reports, we find that structures with the initial rotation angle set at $\theta_0 = 90$ deg exhibit a so-called zero-stiffness mode, with negligible tangential stiffness and trivial resistance force and torque for small deformations [29]. This behavior is consistent with our observation of a broad and nearly flat energy well centered at the origin ($u = 0, \varphi = 0$) for structures with $\theta_0 = 90$ deg. Here, we also use the term, zero-stiffness, to distinguish this behavior from the aforementioned mono-stable and bi-stable cases in our multi-stability diagram. In each panel, the diagram provides the design space of $(h_0/R, \theta_0)$ for creating a bi-stable Kresling truss structure with fixed polygon shape. The upper left region is mono-stable while the lower right is bi-stable. Thus, bi-stability can always be realized by designs with large enough height-to-radius ratio and initial rotation angle. We notice that the bi-stable region is interrupted by a horizontal cap for small values of n . This is caused by the maximum and minimum rotation angle φ the structure could reach, where the crease line trusses start to intersect with each other as mentioned previously. For large n , the accessible φ range increases and the constraint effect of rotation angle on finding a second stable state is suppressed, therefore the cap is gradually

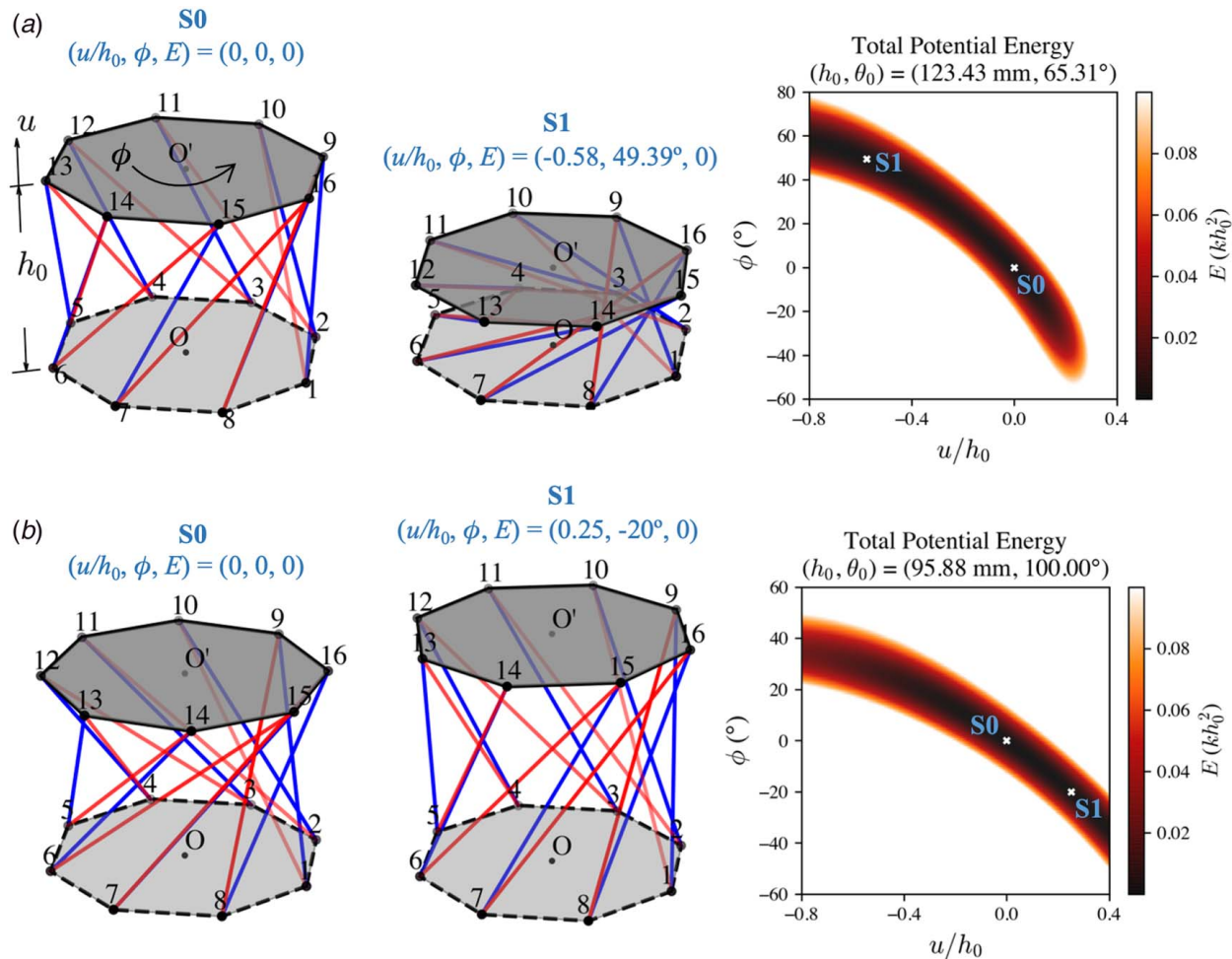


Fig. 4 (a) A bi-stable Kresling truss structure with the second stable state in a contracted shape. Left: initial stable configuration S_0 (u, φ) = (0, 0). Middle: the second stable state S_1 ($-0.58h_0, 49.39$ deg). Right: total potential energy in (u, φ) space. (b) A bi-stable Kresling truss structure with the second stable state in an expanded shape. Left: initial stable configuration S_0 (0, 0). Middle: the second stable state S_1 ($0.25h_0, -20.00$ deg). Right: total potential energy in (u, φ) space. The stable states are denoted by white crosses. Only regions with relatively low energies are shown.

removed. As n increases, the curve separating mono-stability and bi-stability moves towards higher h_0/R and larger θ_0 , which indicates that Kresling truss structures with more vertices generally need higher height-to-radius ratio and larger initial rotation angle to exhibit a second zero-strain configuration within the accessible (u, φ) space. Lastly, we find that for bi-stable Kresling truss structures with $\theta_0 < 90$ deg, the second stable state S_1 always falls in the counter-clockwise contracted quadrant ($u < 0, \varphi > 0$), while for $\theta_0 > 90$ deg, S_1 is found in the clockwise expanded quadrant ($u > 0, \varphi < 0$). Example cases are shown in Figs. 4(a) and 4(b), respectively. This θ_0 -dependent feature is invariant with n .

3.2 Truss-and-Magnet System

3.2.1 Strength of Embedded Permanent Magnets. The magneto-Kresling truss structure incorporates both elastic and the magnetic components where the competition between truss elastic energy and magnetostatic energy plays a critical role in forming the total potential energy profile for a system with a given initial configuration. Here, to pick proper truss-and-magnet strengths, we investigated the number and positions of stable states for an octagon-based ($n=8$) magneto-Kresling truss structure with $R=90$ mm, $(h_0, \theta_0) = (110$ mm, 24 deg) with fixed truss stiffness $k=26.56$ N/m, and varying magnet strength m^2 . More details can be found in the supplemental information note 1 available in the

Supplemental Materials on the ASME Digital Collection regarding the selection of this initial geometry. The result is shown in Fig. 6. Three color schemes were chosen to better visualize the energy gradients in zones with different energy levels. With either very low or very high magnet strength m^2 , the system is mono-stable with only one stable state near the initial configuration having nearly zero potential energy (middle row). With intermediately strong ($0.663 \leq m^2 \leq 0.824$ A² m⁴) magnets embedded, the system could have a second stable state in the clockwise contracted shape (bottom row) and even a third one in the anti-clockwise folded region (top row). For demonstrating how one can find the maximum number of stable states and energy storage capacity, the following discussions are based on the fixed relative strength between trusses and magnets with $k=26.56$ N/m and $m^2=0.785$ A² m⁴. Additionally, radius of the circumscribed circle is kept fixed at $R=90$ mm. These parameters were chosen because they allow us to create tri-stable magneto-Kresling truss structures for certain combinations of h_0 and θ_0 .

To reach magnet strength $m^2=0.785$ A² m⁴, we could use cylindrical permanent magnets with radius $R_m=5$ mm, height $t_m=10$ mm, and residual induction $B_r=1.42$ T. In the published work by Fang et al. [53], the force exerted by a magnetic dipole moment \mathbf{m}_j on another dipole moment \mathbf{m}_i given in Eq. (5) has been tested and validated experimentally using two neodymium-iron-boron (NdFeB) magnets ($R_m=6.35$ mm, $t_m=12.7$ mm, Grade N52 and

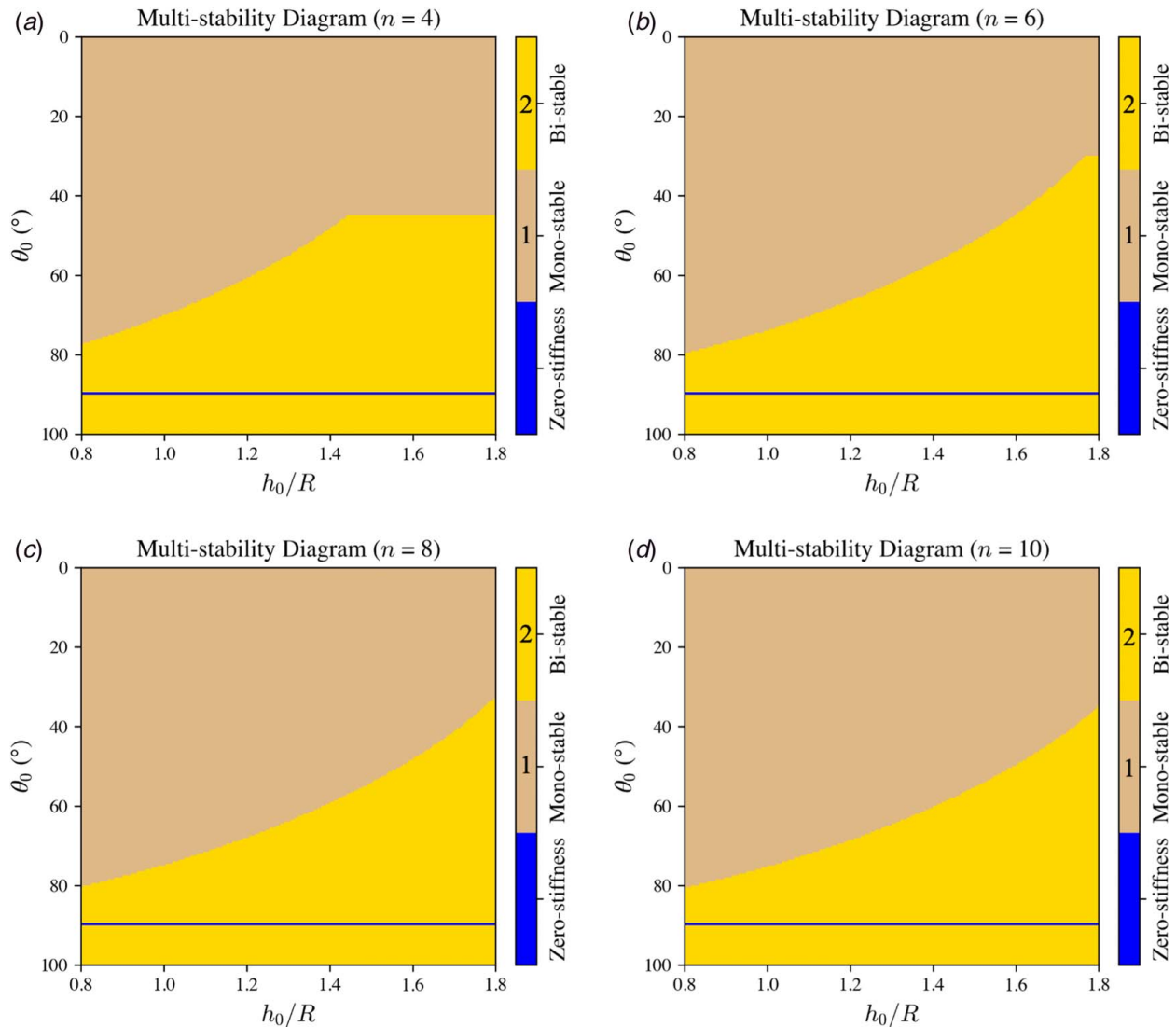


Fig. 5 Multi-stability diagrams showing the number of stable states found numerically for Kresling truss structures with different initial configurations (h_0/R , θ_0) in the domain of interest ($u \geq -0.8h_0$, $\varphi_{\min} \leq \varphi \leq \varphi_{\max}$). Mono-stable and bi-stable regions illustrate cases with one and two stable states, respectively. Zero-stiffness line indicates a special case ($\theta_0 = 90$ deg) where there is a broad and nearly flat energy well surrounding the initial configuration. Diagrams are made for (a) $n = 4$, (b) $n = 6$, (c) $n = 8$, and (d) $n = 10$.

$B_r = 1.44$ T) with the face-to-face distance decreasing from 60 mm to 0 mm. Their findings indicate that the interaction model built on the point dipole assumption can still be used for the close contact of small magnets within negligible error. In our work, we chose to employ smaller magnets with weaker magnetic fields. The constraint of $u \geq -0.8h_0$ keeps the magnet center-to-center distance at least $0.2h_0$ ($h_0 \geq 72$ mm, leading to a face-to-face distance ≥ 4.4 mm). Based on Fang's experiment, the point dipole assumption should hold for our magneto-Kresling truss model. Thus, the energy and force from Eqs. (4) and (5) can be safely applied to evaluate the magneto-static interaction in the distance range of our interest.

3.2.2 Multi-Stability Property of Octagon-Based Magento-Kresling Truss Structures. We extensively studied total potential energy profiles of octagon-based ($n = 8$) magneto-Kresling truss structures and compared them with those of truss-only systems. The changes brought to the potential energy landscape of the truss-only system by magnetostatic interactions can be summarized as follows. First, the number of energy wells encountered along the displacement-controlled zero-torque folding path might be reduced (from mono-stable to unstable and from bi-stable to mono-stable) or increased (from mono-stable to bi-stable) and the energy well

might shift with significant change in well position and depth. For example, total potential energies of a truss-only system and a truss-and-magnet system with the same initial height and rotation angle ($h_0, \theta_0 = (145.47$ mm, 53.06 deg) are shown in Fig. 7(a) left and middle panels, respectively. The two stable states for the truss-only system in the (u, φ) space are $S_0(0, 0)$ and $S_1(-0.61h_0, 73.88$ deg). Both of these states have zero potential energies. For the truss-and-magnet system, the two positions move to $S_0(-0.00158h_0, 0.33$ deg) and $S_1(-0.43h_0, 58.67$ deg) with normalized total potential energy -0.000065 and 0.004714 , respectively. The distance between top- and bottom-layer magnets is relatively large initially, thus weak contributions from the magnetic potential lead to a negligibly small shift of S_0 . In contrast, S_1 is more prominently affected by stronger magnetic interactions as the plates are much closer in this configuration. Since the stable states are no longer zero-strain positions, trusses are stretched in response to the magnetic field. Total potential energies evolving along the two paths are shown in Fig. 7(a) right panel, which clearly exhibits the shift of S_1 in both the well position and well depth.

Additionally, the coupling behavior of vertical displacement and rotation is also altered. Figure 7(b) left and middle panels demonstrate the displacement-controlled zero-torque folding path of a

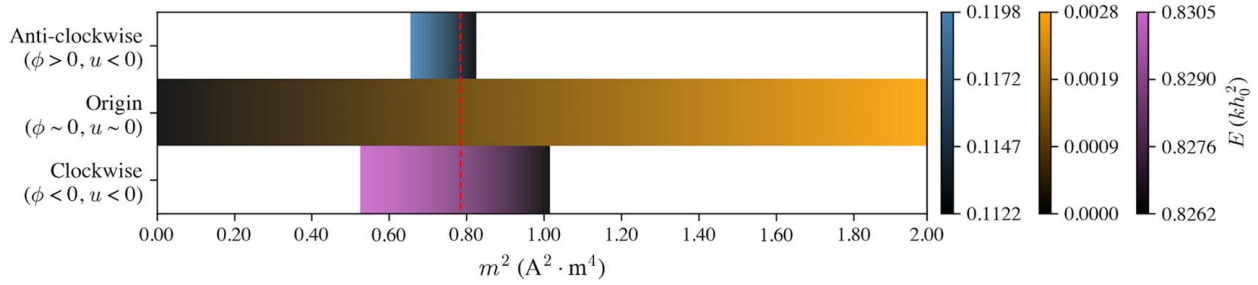


Fig. 6 Changes in the number and region of stable states due to increasing magnetic strength m^2 for an octagon-based ($n = 8$) magneto-Kresling truss structure with $(h_0, \theta_0) = (110 \text{ mm}, 24 \text{ deg})$. Truss strength is kept fixed with stiffness $k = 26.56 \text{ N/m}$. Accessible stable states in the domain of interest ($u \geq -0.8h_0, \varphi_{\min} \leq \varphi \leq \varphi_{\max}$) are divided into three regions based on their deformation (u, φ) with respect to the initial configuration $(0, 0)$. Colors show the normalized total potential energy at each stable state. $m^2 = 0.785 \text{ A}^2 \text{ m}^4$ marked by the dashed line is used for the following discussions. (Color version online.)

truss-only system and a truss-and-magnet system, respectively, with $(h_0, \theta_0) = (108.00 \text{ mm}, 6.10 \text{ deg})$ on the normalized potential energy landscape in the (u, φ) space. In the beginning, top- and bottom-layer magnets are far from each other, thus the folding is driven by elastic trusses, resulting in tiny differences between the two paths before u reaches $-0.5h_0$. As the vertical distance between magnets decreases, magnetic interactions become strong enough to drag the (u, φ) curve of the truss-and-magnet composite system away from that of the truss-only system. In the magnet-and-truss system, the rotation angle φ reaches a maximum value of 68.7 deg , then starts to decrease, and finally stops at 63.4 deg when u approaches $-0.8h_0$, while in the structure without magnets, φ keeps growing and ends up with a final rotation angle of 75.7 deg . To better illustrate this phenomenon, Fig. 7(b) insets show the configurations at $u = -0.8h_0$ for the two structures.

In the final folded configuration of the magneto-Kresling truss system, further rotation pushing node 14 towards node 8 is prohibited by the strong attractive interaction between magnets at nodes 14 and 7. The dominant attractive magnetostatic interactions also lead to a significant decrease in the final total potential energy as shown in Fig. 7(b) right panel. Animations of the folding process for the two structures can be found in Supplemental Materials on the ASME Digital Collection. The deformation path sought by our 2-DOF truss model fits the previous experimental observations better than the pseudo 1-DOF model in terms of the locking effect on the rotation angle caused by favorable magnetic interactions at small heights. Therefore, the difference in (u, φ) coupling behavior between the systems with and without magnets may offer an explanation to the discrepancy seen between experiments and theoretical calculations in prior studies.

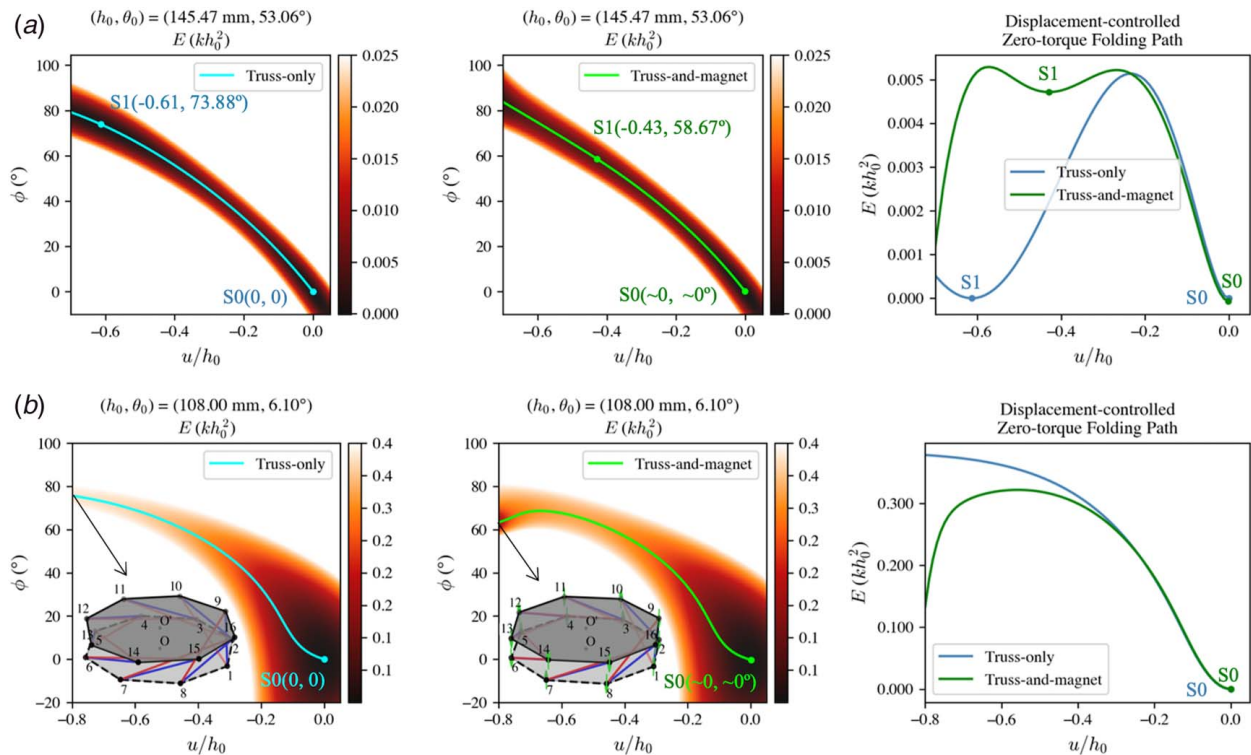


Fig. 7 Comparison of the energy landscape and folding path between the Kresling truss structure and the magneto-Kresling truss structure with the same initial configuration: (a) $(h_0, \theta_0) = (145.47 \text{ mm}, 53.06 \text{ deg})$ and (b) $(h_0, \theta_0) = (108.00 \text{ mm}, 6.10 \text{ deg})$. Left: potential energy landscape of the truss-only system. Middle: potential energy landscape of the truss-and-magnet system. Right: total potential energies along vertical displacement in the displacement-controlled zero-torque folding paths of the truss-only and truss-and-magnet systems. The folding paths starting from $u = 0$ are depicted in solid lines and stable states are marked by solid circles. Insets in (b) are final configurations ($u = -0.8h_0$) in the paths.

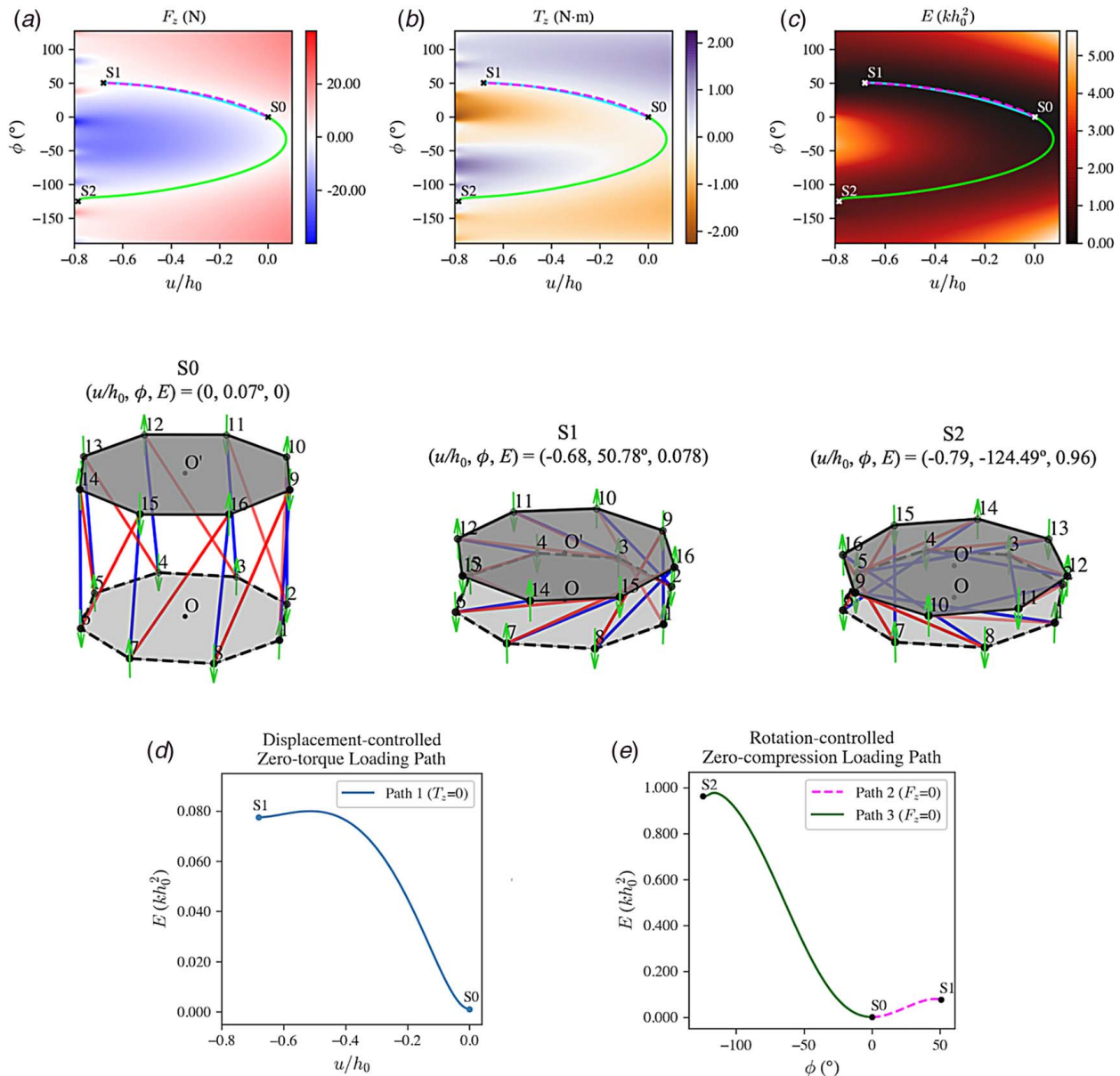


Fig. 8 Top: (a) force F_z , (b) torque T_z applied on the top polygon, (c) normalized total potential energy E in (u, ϕ) space for the octagon-based tri-stable magneto-Kresling truss structure with initial configuration $(h_0, \theta_0) = (107.80 \text{ mm}, 29.66 \text{ deg})$. The solid and dashed curves between S_0 and S_1 show the displacement-controlled zero-torque loading path and the rotation-controlled zero-compression loading path connecting the two states, respectively. The rotation-controlled zero-compression loading path joining S_0 and S_2 is also shown with a solid curve. Middle: three stable configurations corresponding to point S_0 $(u, \phi) = (0.00011h_0, 0.07 \text{ deg})$, S_1 $(-0.68h_0, 50.78 \text{ deg})$ and S_2 $(-0.79h_0, -124.49 \text{ deg})$ in the potential energy landscape. Bottom: change of potential energy along (d) the $T_z = 0$ path from state S_0 to S_1 and (e) the $F_z = 0$ paths from S_0 to S_1 and S_0 to S_2 . (Color version online.)

More interestingly, the magneto-Kresling truss structure with magneto-elastic coupling can be designed to exhibit three stable states, as mentioned previously in justifying our selections on magnet strength. Figure 8 shows details of such an octagon-based magneto-Kresling truss structure with initial configuration $(h_0, \theta_0) = (107.80 \text{ mm}, 29.66 \text{ deg})$. The truss-only system with the same geometry is mono-stable. The magnetic interaction not only pushes the initial potential energy minimum slightly away from the origin to $S_0(0.00011h_0, 0.073 \text{ deg})$ but also brings about extra stable states $S_1(-0.68h_0, 50.78 \text{ deg})$ in the anti-clockwise and $S_2(-0.79h_0, -124.49 \text{ deg})$ in the clockwise folding domains. The normalized total potential energies for configurations S_0 , S_1 , and S_2 are 0.0011, 0.078, and 0.96, respectively. Note that the arrangement of magnetic dipoles is crucial to the existence of these three

stable states because it determines the magneto-elastic coupling by varying the magnetic energy landscape to be superposed onto the elastic potential in the (u, ϕ) space, while the elastic potential profile is fixed for a given initial geometry. We show in multi-stability diagrams (in the supplemental information notes 2, 3, and 4 available in the Supplemental Materials on the ASME Digital Collection) a different alternate layout with top-layer magnets flipped, the attractive layout and the repulsive layout all result in a mono-stable structure for $(h_0, \theta_0) = (107.80 \text{ mm}, 29.66 \text{ deg})$, instead of a tri-stable one discussed here. Under different vertical force and/or torque applied to the top-layer polygon, the system is able to switch from state S_0 to state S_1 along various paths, such as a displacement-controlled loading path with zero-torque (path 1 in solid line connecting S_0 and S_1) or a rotation-

controlled loading path with zero vertical force (path 2 in dashed line connecting S0 and S1). However, it is impossible to find a zero-torque path to switch from state S0 to state S2, because there exists a non-zero-torque region separating S0 and S2 states, as shown in Fig. 8(b). Here, we show a possible rotation-controlled zero-compression loading path (path 3 in solid line connecting S0 and S2) as an example to complete this conformational change. It is evident from these findings that the magneto-Kresling truss is capable of being programed into reaching two or more equilibrium states with different energies under various loading conditions. This path-dependent multi-stability is not observed in the truss-only system. For a Kresling truss structure with an anti-clockwise initial rotation angle ($\theta_0 > 0$), relatively low potential energies always appear in anti-clockwise contracted ($u < 0, \varphi > 0$) or clockwise expanded ($u > 0, \varphi < 0$) quadrants as shown in Figs. 4(a) and 4(b) right panels. There is no energy minimum in the clockwise contracted ($u < 0, \varphi < 0$) or anti-clockwise expanded ($u > 0, \varphi > 0$) regions due to strains induced in truss members in those two regions. As a result, all of the potential energy minima with zero strain can be found along the displacement-controlled zero-torque path connecting the deformation space. However, an extra local energy minimum with zero-force and zero-torque located in the relatively high-energy region with $u < 0$ and $\varphi < 0$ could arise in a magnet-and-truss system if magnetic interactions are strong enough to counteract forces coming from heavily stretched truss members. With these considerations, we can classify the potential energy minima into two categories based on the stress state of truss members. Class 1 minimum describes cases with slightly stretched truss members, and class 2 minimum involves heavily stretched ones. Along a zero-torque loading path starting from the initial configuration, every low-energy class 1 minimum can be visited, whereas the class 2 local minimum is inaccessible in the absence of torque. This classification helps with our following discussion about the multi-stability diagram of the magneto-Kresling truss structures. It should be noted that we exclude extremely low-energy states where two layers of magnets are in close contact with each other since this may violate the magnetic point dipole assumption and may not be functional given the large forces needed to reset the system to another state. Thus, we restrict our attention to cases with $u \geq -0.8h_0$. Such a limit on displacement can be adopted in experiments using springs or soft contacts to keep the top and bottom plates sufficiently apart. To prove S0, S1, and S2 are equilibrium positions, the structure would finally rest at under a small perturbation introduced to the system, we carried out dynamic tests numerically by releasing the structure from a position very close to any of the three states with zero initial velocity and observed that the system ended up staying at the desired energy well after a short period of damped free vibration. Details can be found in the supplemental information note 5 available in the [Supplemental Materials](#) on the ASME Digital Collection.

3.2.3 Effect of Different Polygon Shapes and Energy Storage Capacity. For Kresling truss structures with n -sided polygons, the number of stable states is only determined by height-to-radius ratio h_0/R and initial rotation angle θ_0 . However, with the same n , the interplay between multi-stability the property of the magneto-Kresling truss structure and design parameters is much more complicated, involving the height h_0 , radius R , initial rotation angle θ_0 , truss stiffness k , magnetic moment magnitude m , and magnet arrangement. Note that it is the absolute values of height and radius that affect the potential energy landscape of the magnet-and-truss system, rather than the ratio of them. This is reasonable because as the model dimensions are increased, the magnet interactions eventually become negligible unless the magnet sizes and strengths are also scaled proportionally. The full multi-stability diagram of the truss-and-magnet system should be in a high-dimensional space with all of the geometry and strength variables considered. Here, we fix the geometry parameter R , strength parameter k and m^2 , and magnet arrangement as those in the previous

section such that we can obtain 2D multi-stability diagrams with $n = 4, 6, 8,$ and 10 for magneto-Kresling truss structures to study the dependence of number of stable states on initial height h_0 and rotation angle θ_0 with different polygon shapes and compare them with the truss-only system in Sec. 3.1.2. As shown in Fig. 9, initial configurations with different numbers of stable states are not simply separated by one or two curves, which is the case for the truss-only system. The (h_0, θ_0) space is divided into several pieces and the zero-stiffness case is removed. Besides the change of mono-stability and bi-stability regions, the magnetostatic interaction also creates unstable structures. The structure becomes unstable when the potential energy well of the purely elastic Kresling truss structure is replaced by a saddle point. As n increases from 6 to 10, the unstable region moves in the direction of smaller height and rotation angle with diminishing area. Additionally, tri-stability is observed for $n = 8$ under our current selection of $R, k, m^2,$ and magnet layout.

To better understand the role of n in forming the multi-stability, we break down the regions of bi-stable and tri-stable cases according to the types of minima each structure has. We exclude unstable and mono-stable systems from our discussion because they do not possess multiple local minima with distinct energy levels to facilitate functions such as energy storage upon deformation-induced switching. Also, we ignore disjointed scattered multi-stable points because the desired initial configurations could be inevitably missed within fabrication error, such as the point near $\theta_0 = 0$ boundary with $(h_0, \theta_0) = (114.97 \text{ mm}, 1.51 \text{ deg})$ in Fig. 9(a). The multi-stability decomposition result is shown in Fig. 10. Class 1 and class 2 minima were defined previously. For small values of n ($n = 4$ and 6), we just observe regions of bi-stable structures with two class 1 minima where trusses are slightly stretched. For $n = 8$ and 10 , class 2 minimum in the ($u < 0, \varphi < 0$) quadrant with heavily stretched truss members comes into the picture. As shown in Figs. 10(c) and 10(d), the bi-stable point is made up of either two class 1 minima or one class 1 minimum and one class 2 minimum. As n increases, the contribution of the rotational periodicity of magnetostatic energy to creating total potential energy minima increases because the range of accessible φ values broadens, and various favorable states are introduced with increasing magnet pairs. This is evident from the numerous valleys and hills formed near $u = -0.8h_0$ in the force and torque plots in Figs. 8(a) and 8(b). These valleys and hills become apparent when the two plates are in close proximity and this is key to generating class 2 local energy minima. Furthermore, for $n = 8$, the two types of bi-stable bands intersect with each other thus creating tri-stability in the intersections. However, those two bands get well separated when $n = 10$, thus failing to generate a shared region with three stable states. In conclusion, the appearance of tri-stability requires both large enough n to develop class 2 minimum and also the intersection of regions with one class 2 minimum and two class 1 minima.

Finally, turning our attention to applications of these multi-stable systems, we investigated how the design parameters influence the maximum amount of energy that can be stored, ΔE_{\max} , when these systems are deformed. The results for parametric sweeps for initial height h_0 , rotation angle θ_0 , and number of edges, n , are summarized in Fig. 11. ΔE_{\max} is defined as the maximum value of total potential energy difference (normalized by kh_0^2) between any of the two stable states a structure could rest at without external force and torque, which amounts to the work expended in switching between these two states. Unstable and mono-stable structures cannot store energy, thus have $\Delta E_{\max} = 0$. We find that for structures with $n = 4$ and 6 , the energy storage capacity is generally much smaller than those with larger values of n . This is related to the emergence of the class 2 minimum with relatively large strain energy resulting from heavily stretched truss members in structures with $n = 8$ and 10 . The highlighted regions in Figs. 11(c) and 11(d) are reminiscent of the bands with a class 2 minimum in Figs. 10(c) and 10(d), respectively. For multi-stable octagon-based ($n = 8$) magneto-Kresling truss

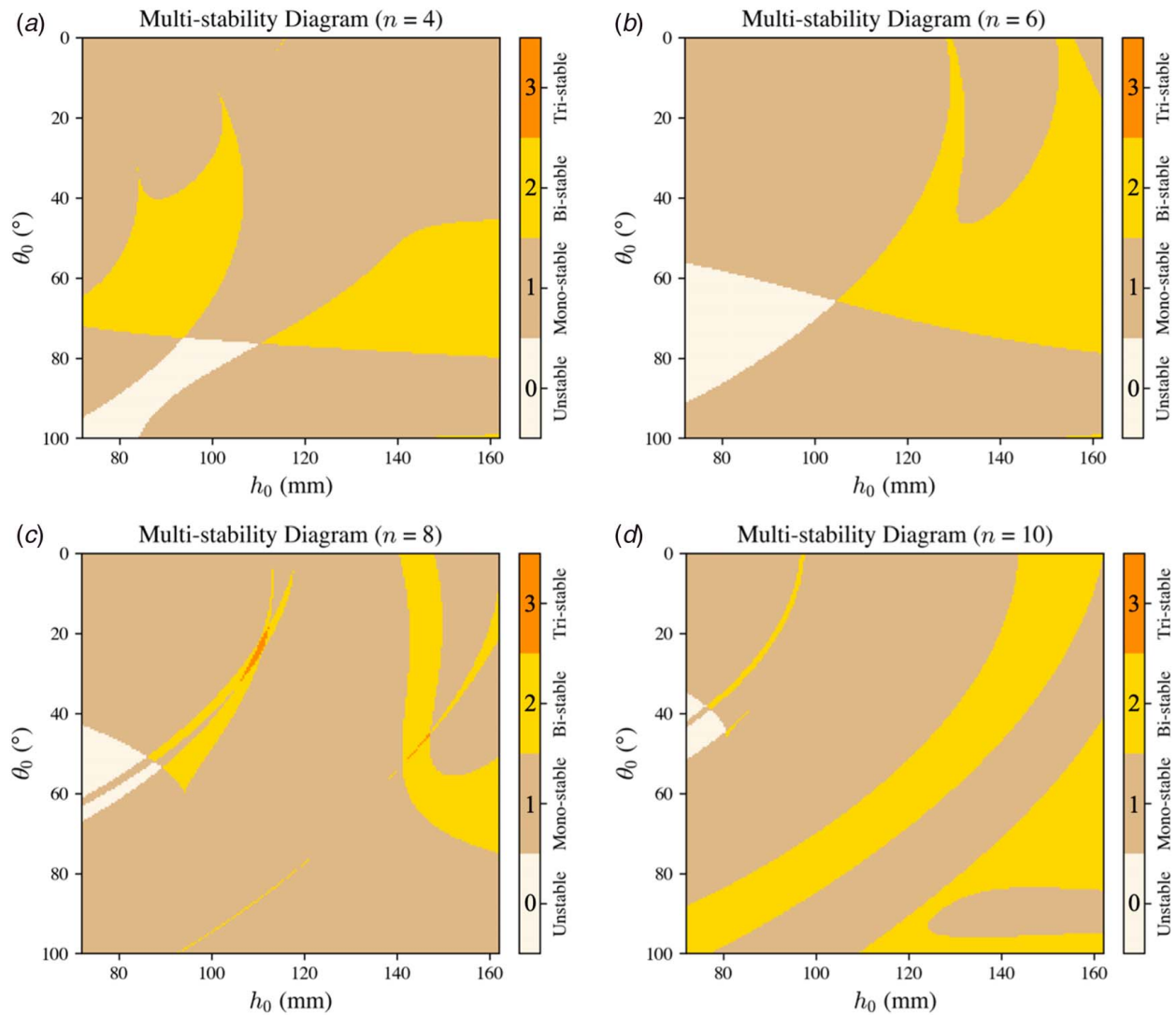


Fig. 9 Multi-stability diagrams showing the number of stable states found numerically for magneto-Kresling truss structures with different initial configurations (h_0, θ_0) in the domain of interest ($u \geq -0.8h_0, \varphi_{\min} \leq \varphi \leq \varphi_{\max}$). Unstable, mono-stable, bi-stable, and tri-stable regions illustrate cases with zero, one, two, and three stable states, respectively. Diagrams are made for (a) $n=4$, (b) $n=6$, (c) $n=8$, and (d) $n=10$ with $R=90$ mm, $k=26.56$ N/m, and $m^2=0.785$ A² m⁴. Nodal magnets take opposite dipole moment directions as shown in Fig. 3(c).

systems, the structure with initial configuration $(h_0, \theta_0) = (86.47$ mm, 50.75 deg) has the maximum energy storage capacity $\Delta E_{\max} = 2.25$ (measured in kh_0^2), which amounts to an energy density of 0.297 J/L (see supplemental information note 6 available in the [Supplemental Materials](#) on the ASME Digital Collection). A deformation path from the linear interpolation between its two stable states is depicted and animated in the [Supplemental Material](#) on the ASME Digital Collection. Starting from its initial stable state, a prescribed force and torque quasi-statically compress and rotate this magneto-Kresling truss structure and finally lock it at a heavily deformed stable configuration with much higher potential energy when the force and torque are removed. To put our findings into a broader context, we introduce two scaling factors for the magneto-Kresling truss structure, the geometry coefficient, C_{geo} , and the strength coefficient, C_{str} . Fixing the polygon shape and magnet arrangement, the system with initial height h_0 , radius R , truss stiffness k , and magnet strength m^2 would have the same normalized potential energy landscape as the system with initial height $C_{\text{geo}} \cdot h_0$, radius $C_{\text{geo}} \cdot R$, truss stiffness $C_{\text{str}} \cdot k$, and magnet strength $C_{\text{str}}^2 \cdot m^2$, indicated by the elastic energy and magnetostatic energy described in Eqs. (3) and (6), respectively. This scaling law sheds light on tuning the energy storage capacity and

miniaturizing the truss-and-magnet system without altering the normalized energy landscape.

4 Discussion

We believe that the magneto-Kresling truss structure we established offers insights into the development of origami-based metamaterials. Possible engineering applications may take advantage of its multi-stability property, which is particularly useful for mechanical switches, energy storage, and harvesting, among other applications. Compared with the previously proposed magneto-origami structure, the truss-based design shows the similar behavior in terms of quantitatively shifting the stable states and changing energy well depths of the system without magnets. The zero-height configuration with favorable magnetic interactions was reported as an additional stable state of the magneto-origami structure in their numerical calculations. This low-energy configuration also appears in our magneto-Kresling truss structure when the magnets in the top layer get close contact with those in the bottom layer and create strong adhesion, but this state is not counted in our multi-stability analysis as mentioned previously. The truss system in our

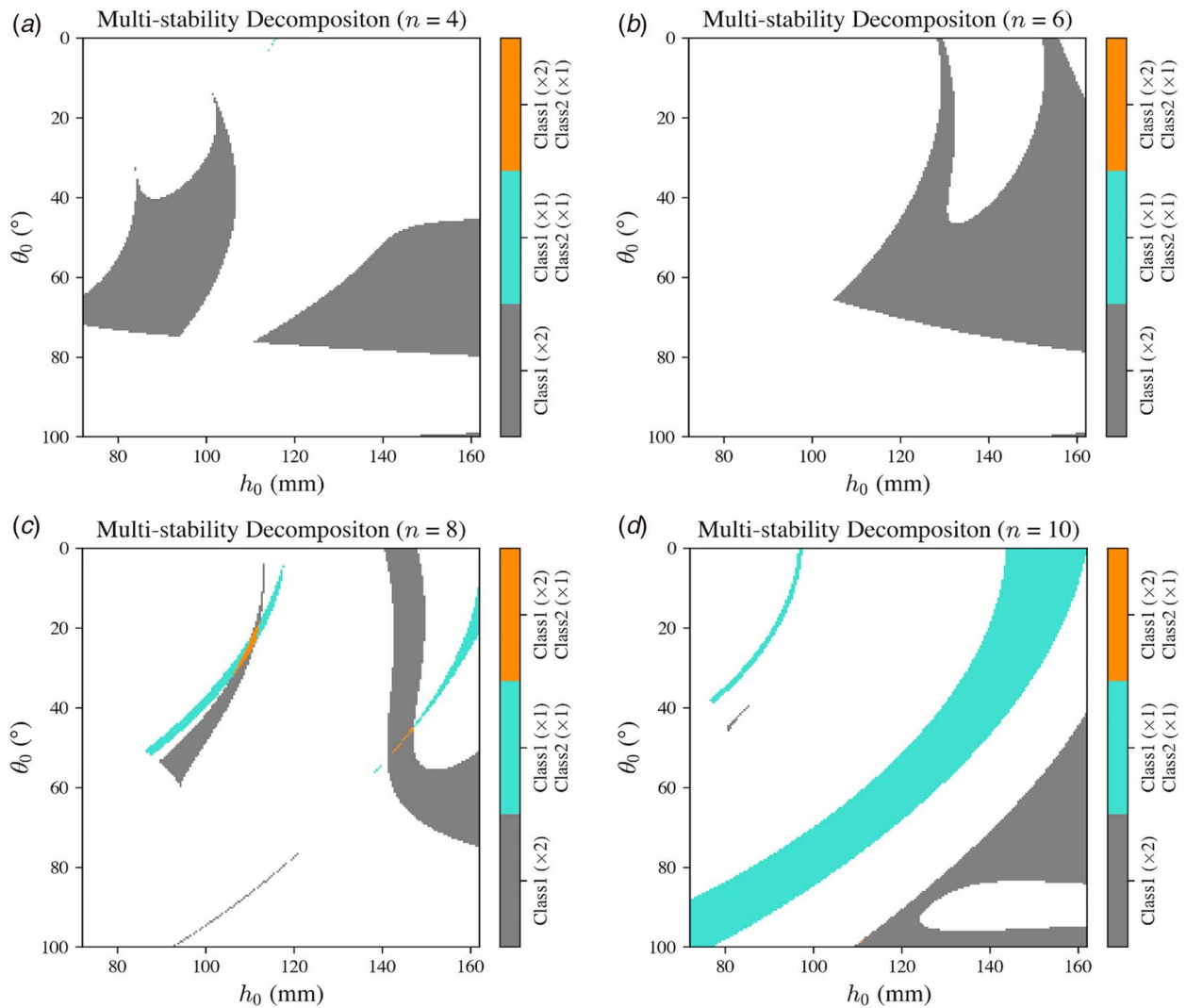


Fig. 10 Decomposition of the multi-stability diagram in Fig. 9 to classify potential energy minima of multi-stable magneto-Kresling truss structures. Class 1 and class 2 minimum are defined as the stable state with slightly and heavily stretched truss members, respectively. Bi-stable structures could have either two class 1 minima or one class 1 minimum and one class 2 minimum. Tri-stable structures possess two class 1 minima and one class 2 minimum. Diagrams are made for (a) $n = 4$, (b) $n = 6$, (c) $n = 8$, and (d) $n = 10$. (Color version online.)

design enables coupling the vertical displacement and rotation angle in a way controlled by the input force and torque thus making it possible to visit different stable states along various deployment paths and create a tri-stable structure with an extra stable state not discovered in previous findings. Embedding permanent magnets in the purely elastic frame to trigger the magneto-elastic coupling endows the magneto-Kresling truss structure with unprecedented versatility relative to designs focusing on elastic components only. Our investigation of the path-dependent multi-stability property and highly tunable potential energy landscape partly unravels the complicated mechanical performance of the magneto-Kresling truss structure. Further exploration could focus on prototype fabrication and experimental validation, to overcome possible challenges such as buckling of slender members or other failure mechanisms [36]. Although the magneto-Kresling truss structure proposed herein was envisioned for macroscale applications, it would also be interesting to find its microscale counterparts. It has been discovered that the α -helical barrel structure of the transmembrane domain of the large conductance mechanosensitive ion channel (MscL) shares similar shape and structural characteristics with the Kresling origami [61]. Moreover, our idea of using complementary magnetic interactions to create hills and valleys along the deformation path is also used in tough structural biomaterials

like spider silk, where complementary electrostatic interactions such as hydrogen bonds in beta-sheets and beta-helices also exhibit similar energy landscapes [51,52]. Realizing the analogy between proteins and origami, the origami-inspired structure is a promising platform for scaling up the mechanisms seen in proteins.

We note that the focus herein was the static or quasi-static deformations. The dynamic behavior of the 1D chain and 2D lattice made up of Kresling truss units has been recently studied with respect to its low-amplitude wave propagation property [9–11]. The chaotic dynamics of a two-unit composite subjected to base excitations can be predicted by the machine learning technique [62]. The deployment dynamics of a single bi-stable unit and multiple bi-stable units is demonstrated via releasing the structure at different heights and recording the final configurations [55]. However, the unit cell in response to different dynamic loadings and the effect of the initial configuration still remain largely unexplored due to the complexity from the multi-stability and strong nonlinearity [26,30,63]. A thorough study of the dynamic behavior of the truss-only structure and its extension to the magneto-Kresling truss system could be useful to prospect these systems for acoustic and mechanical metamaterials applications.

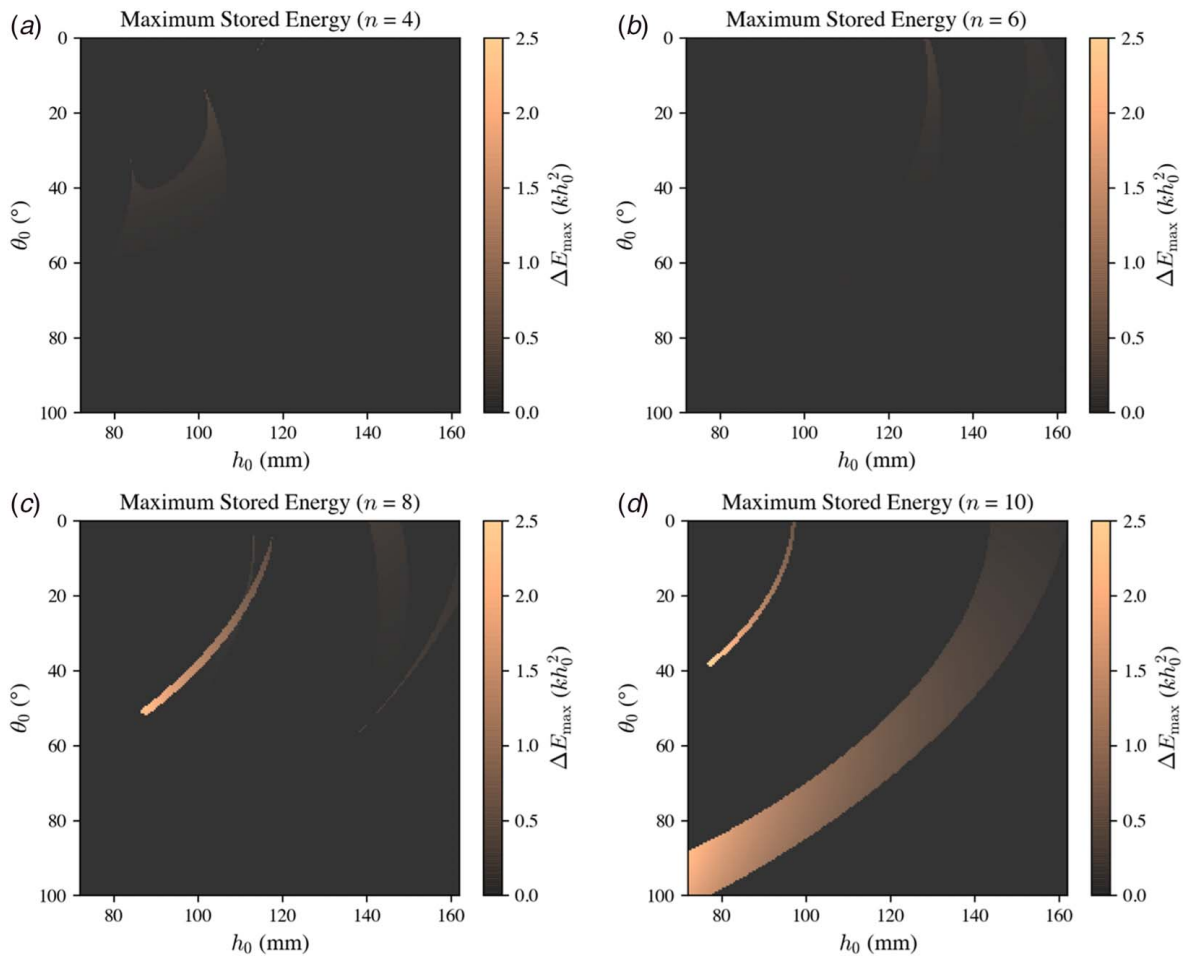


Fig. 11 Maximum normalized energy ΔE_{\max} that can be stored in magneto-Kresling truss systems with different initial configurations (h_0, θ_0) . Energy stored amounts to the work expended in snapping between two stable states in the domain of interest ($u \geq -0.8h_0$, $\varphi_{\min} \leq \varphi \leq \varphi_{\max}$). Diagrams are made for (a) $n = 4$, (b) $n = 6$, (c) $n = 8$, and (d) $n = 10$ with $R = 90$ mm, $k = 26.56$ N/m, and $m^2 = 0.785$ A² m⁴. Nodal magnets take opposite dipole moment directions as shown in Fig. 3(c).

5 Conclusions

Kresling truss structure, a derivative of Kresling origami cylinder, is a popular unit cell in forming origami-inspired metamaterials. Taking inspiration from biological structures found in proteins, we presented a magneto-elastic system by embedding nodal magnets in the top and bottom polygons of the Kresling truss structure with alternate point dipole directions and then extensively investigated its rich patterns of the potential energy landscape resulting from coupled elastic and magnetostatic energies. We primarily focused on the multi-stability property of the magneto-Kresling truss structure and described how design parameters such as the initial configuration, polygon shape, and magnet properties influence the behavior. Unlike the truss-only system with uniform truss stiffness, the multi-well potential energy profile of the magneto-Kresling truss structure not only relies on its geometry but also rests with the relative strength of the constituent truss and magnet. We illustrated that the octagon-based magneto-Kresling truss structure with nodal magnets could transform the elastic structure from bi-stable to mono-stable, and vice versa, or produce an unstable structure. The magnetic interaction could also shift the local minimum energy position and change the energy well depth. We demonstrated the vertical displacement and rotation coupling is different for the truss-only and the truss-and-magnet systems, an aspect that was not explored before and may explain previously observed discrepancies between theory and experiments. In our efforts to probe the possibility of multi-stability in these systems, we emphasized that the quasi-static

transition paths joining different stable states should not be limited to the commonly studied zero-torque pathway, where only the axial compression or tension is applied. In particular, we show that a rotation-controlled loading path without axial forces also exists. This turns out to be a crucial aspect, as it allows us to detect initial configurations resulting in three stable states for the magneto-Kresling truss structure. Specifically, the third stable state with the highest potential energy among all of the three local minima can only be reached from other stable states when an external torque is applied. This tri-stability feature is missing for the truss-only system. In the end, we show that the magnetostatic interaction enables the energy storage by converting the zero-strain stable state of the truss-only structure into either a slightly stressed or a heavily stressed one. The amount of energy trapped or released during the switch could be adjusted by various geometry and strength design parameters. This highly tunable energy storage capacity intrinsic to our proposed magnet arrangements of the multi-stable magneto-Kresling truss structure exemplifies potential advantages of magneto-elastic designs over the traditional purely elastic Kresling truss structure.

Acknowledgment

The authors acknowledge the support from the Department of Civil and Environmental Engineering and Mechanical Engineering at Northwestern University, as well as the Northwestern University High Performance Computing Center for a supercomputing grant.

Conflict of Interest

There are no conflicts of interest.

Data Availability Statement

The datasets generated and supporting the findings of this article are obtained from the corresponding author upon reasonable request. The authors attest that all data for this study are included in the paper.

Funding Data

- National Science Foundation (Grant No. CMMI-2034584; Funder ID: 10.13039/501100001809).

Nomenclature

m = magnitude of magnetic dipole moment \mathbf{m}
 u = vertical displacement of the top polygon in the deployment
 M = saturation magnetization of the magnet
 N = number of vertices (or nodes) of each polygon
 R = radius of the circumscribed circle of the n -sided regular polygon
 V = number of trusses connecting the top and bottom polygons
 \mathbf{B} = structure strain–displacement matrix with size $6N \times V$
 \mathbf{P} = nodal force matrix with size $6N \times 1$
 \mathbf{R} = rotation matrix with size 3×3
 a_0 = initial length of mountain creases
 b_0 = initial length of valley creases
 $e_{\text{mag},ij}$ = magnetostatic energy between magnetic dipole at node i and magnetic dipole at node j
 h_0 = initial height of the Kresling or magneto-Kresling truss structure
 k_v = stiffness of the v th truss
 l_v = length of the v th truss
 l_{v0} = initial length of the v th truss
 q_v = force of the v th truss (entry of \mathbf{Q}_f)
 r_{ij} = magnitude of vector \mathbf{r}_{ij}
 t_m = height of embedded cylindrical permanent magnets
 $\mathbf{f}_{\text{mag},ij}$ = magnetic force felt by magnetic dipole at node i from magnetic dipole at node j
 \mathbf{m}_i = magnetic point dipole moment at node i with size 3×1
 \mathbf{r}_{ij} = the vector from node i to node j with size 3×1
 B_r = material residual induction of the magnet
 C_{geo} = scaling factor for the geometry parameters
 C_{str} = scaling factor for the strength parameters
 E_{el} = total elastic energy from the truss deformation
 E_{mag} = total magnetostatic energy involving all inter-layer magnet pairs
 E_{tot} = total potential energy
 F_z = total force along z -axis acting on the top polygon to equilibrate the structure undergoing deformation (u, φ)
 $F_{i,j}$ = force applied on node i in j -dir (entry of \mathbf{P})
 $F_{z,el}$ = force along z -axis acting on the top polygon in response to the truss deformation
 $F_{z,\text{mag}}$ = force along z -axis acting on the top polygon to resist the magnetic interactions
 R_m = radius of embedded cylindrical permanent magnets
 $T_{z,el}$ = torque about z -axis acting on the top polygon in response to the truss deformation
 $T_{z,\text{mag}}$ = torque about z -axis acting on the top polygon to resist the magnetic interactions
 T_z = total torque about z -axis acting on the top polygon to equilibrate the structure undergoing deformation (u, φ)
 \mathbf{B}_v = element strain–displacement matrix for the v th truss with size $6N \times V$

$\mathbf{F}_{\text{mag},w}$ = magnetic force felt by magnetic dipole at node w
 \mathbf{Q}_f = element force matrix with size $V \times 1$
 \mathbf{U}_f = nodal position matrix with size $2N \times 3$
 Vol = volume of the magnet
 ΔE_{max} = maximum energy (normalized by kh_0^2) can be stored in a magneto-Kresling truss structure
 $\Delta \mathbf{U}$ = nodal displacement matrix with size $2N \times 3$
 θ = relative rotation angle offset by the top and bottom polygons
 θ_0 = initial relative rotation angle offset by the top and bottom polygons
 μ_0 = permeability of vacuum
 φ = rotation angle of the top polygon in the deployment
 φ_{max} = maximum rotation angle of the top polygon due to the intersection of valley creases
 φ_{min} = minimum rotation angle of the top polygon due to the intersection of mountain creases

References

- Turner, N., Goodwine, B., and Sen, M., 2016, "A Review of Origami Applications in Mechanical Engineering," *Proc. Inst. Mech. Eng. Part C J. Mech. Eng. Sci.*, **230**(14), pp. 2345–2362.
- Miyashita, S., Guitron, S., Yoshida, K., Shuguang, L., Damian, D. D., and Rus, D., 2016, "Ingestible, Controllable, and Degradable Origami Robot for Patching Stomach Wounds," IEEE International Conference on Robotics and Automation (ICRA), Stockholm, Sweden, May 16–21, pp. 909–916.
- Sargent, B., Butler, J., Seymour, K., Bailey, D., Jensen, B., Magleby, S., and Howell, L., 2020, "An Origami-Based Medical Support System to Mitigate Flexible Shaft Buckling," *ASME J. Mech. Rob.*, **12**(4), p. 041005.
- Johnson, M., Chen, Y., Hovet, S., Xu, S., Wood, B., Ren, H., Tokuda, J., and Tse, Z. T. H., 2017, "Fabricating Biomedical Origami: A State-of-the-Art Review," *Int. J. Comput. Assist. Radiol. Surg.*, **12**(11), pp. 2023–2032.
- Seymour, K., Burrow, D., Avila, A., Bateman, T., Morgan, D. C., Magleby, S. P., and Howell, L. L., 2018, "Origami-Based Deployable Ballistic Barrier," Origami7: Seventh International Meeting of Origami Science, Mathematics, and Education, R. Lang, M. Bolitho, and Z. You, eds., Vol. 3, Tarquin, St. Albans, pp. 763–777.
- Morgan, J., Magleby, S. P., and Howell, L. L., 2016, "An Approach to Designing Origami-Adapted Aerospace Mechanisms," *ASME J. Mech. Des.*, **138**(5), p. 052301.
- Pehrson, N. A., Ames, D. C., Smith, S. P., Magleby, S. P., and Arya, M., 2020, "Self-Deployable, Self-Stiffening, and Retractable Origami-Based Arrays for Spacecraft," *AIAA J.*, **58**(7), pp. 3221–3228.
- Wu, R., Roberts, P. C. E., Soutis, C., and Diver, C., 2018, "Heliogyro Solar Sail With Self-Regulated Centrifugal Deployment Enabled by an Origami-Inspired Morphing Reflector," *Acta Astronaut.*, **152**, pp. 242–253.
- Yasuda, H., Miyazawa, Y., Charalampidis, E. G., Chong, C., Kevrekidis, P. G., and Yang, J., 2019, "Origami-Based Impact Mitigation Via Rarefaction Solitary Wave Creation," *Sci. Adv.*, **5**(5), pp. eaau2835–eaau2835.
- Yasuda, H., and Yang, J., 2017, "Tunable Frequency Band Structure of Origami-Based Mechanical Metamaterials," *J. Int. Assoc. Shell Spatial Struct.*, **58**(4), pp. 287–294.
- Wu, Y., Chaunsali, R., Yasuda, H., Yu, K., and Yang, J., 2018, "Dial-In Topological Metamaterials Based on Bistable Stewart Platform," *Sci. Rep.*, **8**(1), pp. 112–112.
- Hang, Y., and Li, M., 2019, "Multi-Stable Mechanical Metamaterials by Elastic Buckling Instability," *J. Mater. Sci.*, **54**(4), pp. 3509–3526.
- He, C., Lai, H.-S., He, B., Yu, S.-Y., Xu, X., Lu, M.-H., and Chen, Y.-F., 2020, "Acoustic Analogues of Three-Dimensional Topological Insulators," *Nat. Commun.*, **11**(1), pp. 2318–2318.
- Li, S., Fang, H., Sadeghi, S., Bhovad, P., and Wang, K., 2019, "Architected Origami Materials: How Folding Creates Sophisticated Mechanical Properties," *Adv. Mater.*, **31**(5), p. e1805282.
- Boatti, E., Vasios, N., and Bertoldi, K., 2017, "Origami Metamaterials for Tunable Thermal Expansion," *Adv. Mater.*, **29**(26), pp. 1700360.
- Yasuda, H., and Yang, J., 2015, "Reentrant Origami-Based Metamaterials With Negative Poisson's Ratio and Bistability," *Phys. Rev. Lett.*, **114**(18), pp. 185502–185502.
- Kochmann, D. M., and Bertoldi, K., 2017, "Exploiting Microstructural Instabilities in Solids and Structures: From Metamaterials to Structural Transitions," *ASME Appl. Mech. Rev.*, **69**(5), p. 050801.
- Leelavanichkul, S., Cherkaev, A., Adams, D. O., and Solzbacher, F., 2010, "Energy Absorption of a Helicoidal Bistable Structure," *J. Mech. Mater. Struct.*, **5**(2), pp. 305–321.
- Shan, S., Kang, S. H., Raney, J. R., Wang, P., Fang, L., Candido, F., Lewis, J. A., and Bertoldi, K., 2015, "Multistable Architected Materials for Trapping Elastic Strain Energy," *Adv. Mater.*, **27**(29), pp. 4296–4301.
- Xiang, X. M., Lu, G., and You, Z., 2020, "Energy Absorption of Origami Inspired Structures and Materials," *Thin Walled Struct.*, **157**, p. 107130.
- Harne, R. L., Thota, M., and Wang, K. W., 2013, "Concise and High-Fidelity Predictive Criteria for Maximizing Performance and Robustness of Bistable Energy Harvesters," *Appl. Phys. Lett.*, **102**(5), p. 053903.

- [22] Hwang, M., and Arrieta, A. F., 2018, "Input-Independent Energy Harvesting in Bistable Lattices From Transition Waves," *Sci. Rep.*, **8**(1), pp. 3630–3639.
- [23] Kim, J., Dorin, P., and Wang, K. W., 2020, "Vibration Energy Harvesting Enhancement Exploiting Magnetically Coupled Bistable and Linear Harvesters," *Smart Mater. Struct.*, **29**(6), p. 65006.
- [24] Wang, P., Shim, J., and Bertoldi, K., 2013, "Effects of Geometric and Material Nonlinearities on Tunable Band Gaps and Low-Frequency Directionality of Phononic Crystals," *Phys. Rev. B: Condens. Matter*, **88**(1), p. 014304.
- [25] Johnson, D. R., Harné, R. L., and Wang, K. W., 2014, "A Disturbance Cancellation Perspective on Vibration Control Using a Bistable Snap-Through Attachment," *ASME J. Vib. Acoust.*, **136**(3), p. 031006.
- [26] Zhang, M., Yang, J., and Zhu, R., 2021, "Origami-Based Bistable Metastructures for Low-Frequency Vibration Control," *ASME J. Appl. Mech.*, **88**(5), p. 051009.
- [27] Harné, R. L., and Wang, K. W., 2017, *Harnessing Bistable Structural Dynamics for Vibration Control, Energy Harvesting and Sensing*, John Wiley and Sons, Hoboken, NJ.
- [28] Ishida, S., Uchida, H., Shimosaka, H., and Hagiwara, I., 2017, "Design and Numerical Analysis of Vibration Isolators With Quasi-Zero-Stiffness Characteristics Using Bistable Foldable Structures," *ASME J. Vib. Acoust.*, **139**(3), p. 031015.
- [29] Yasuda, H., Tachi, T., Lee, M., and Yang, J., 2017, "Origami-Based Tunable Truss Structures for Non-Volatile Mechanical Memory Operation," *Nat. Commun.*, **8**(1), pp. 962–962.
- [30] Masana, R., Khazaaleh, S., Alhussein, H., Crespo, R. S., and Daqaq, M. F., 2020, "An Origami-Inspired Dynamically Actuated Binary Switch," *Appl. Phys. Lett.*, **117**(8), p. 81901.
- [31] Jianguo, C., Xiaowei, D., Ya, Z., Jian, F., and Yongming, T., 2015, "Bistable Behavior of the Cylindrical Origami Structure With Kresling Pattern," *ASME J. Mech. Des.*, **137**(6), p. 061406.
- [32] Li, M., Zhang, J. Z. H., and Xia, F., 2016, "A New Algorithm for Construction of Coarse-Grained Sites of Large Biomolecules," *J. Comput. Chem.*, **37**(9), pp. 795–804.
- [33] Tlustý, T., Libchaber, A., and Eckmann, J.-P., 2017, "Physical Model of the Genotype-to-Phenotype Map of Proteins," *Phys. Rev. X*, **7**(2), p. 021037.
- [34] Rocks, J. W., Pashine, N., Bischofberger, I., Goodrich, C. P., Liu, A. J., and Nagel, S. R., 2017, "Designing Allostery-Inspired Response in Mechanical Networks," *Proc. Natl. Acad. Sci. USA*, **114**(10), p. 2520–2525.
- [35] Zhang, Q., Wang, X., Cai, J., and Feng, J., 2021, "Motion Paths and Mechanical Behavior of Origami-Inspired Tunable Structures," *Mater. Today Commun.*, **26**, p. 101872.
- [36] Masana, R., and Daqaq, M. F., 2019, "Equilibria and Bifurcations of a Foldable Paper-Based Spring Inspired by Kresling-Pattern Origami," *Phys. Rev. E*, **100**(6-1), p. 063001.
- [37] Farshad, M., and Benine, A., 2004, "Magnetoactive Elastomer Composites," *Polym. Test.*, **23**(3), pp. 347–353.
- [38] Bira, N., Dhagat, P., and Davidson, J. R., 2020, "A Review of Magnetic Elastomers and Their Role in Soft Robotics," *Front. Rob. AI*, **7**, pp. 588391–588391.
- [39] Kavlicoglu, B., Wallis, B., Sahin, H., and Liu, Y., 2011, "Magnetorheological Elastomer Mount for Shock and Vibration Isolation," *SPIE Smart Structures and Materials: Active and Passive Smart Structures and Integrated Systems*, San Diego, CA, Apr. 27, Vol. 7977, p. 79770Y.
- [40] John, G., Schlotter, W., and Nichols, M., 2001, "Magnetorheological Elastomers in Tunable Vibration Absorbers," *SPIE Smart Structures and Materials: Damping and Isolation*, Newport Beach, CA, July 2, Vol. 4331, pp. 103–110.
- [41] Harné, R. L., Deng, Z., and Dapino, M. J., 2018, "Adaptive Magnetoelastic Metamaterials: A New Class of Magnetorheological Elastomers," *J. Intell. Mater. Syst. Struct.*, **29**(2), pp. 265–278.
- [42] Leng, D., Wu, T., Liu, G., Wang, X., and Sun, L., 2018, "Tunable Isolator Based on Magnetorheological Elastomer in Coupling Shear-Squeeze Mixed Mode," *J. Intell. Mater. Syst. Struct.*, **29**(10), pp. 2236–2248.
- [43] Kim, Y., Yuk, H., Zhao, R., Chester, S. A., and Zhao, X., 2018, "Printing Ferromagnetic Domains for Untethered Fast-Transforming Soft Materials," *Nature*, **558**(7709), pp. 274–279.
- [44] Kim, Y., Parada, G. A., Liu, S., and Zhao, X., 2019, "Ferromagnetic Soft Continuum Robots," *Sci. Rob.*, **4**(33), p. eaax7329.
- [45] Hellebrekers, T., Chang, N., Chin, K., Ford, M., Kroemer, O., and Majidi, C., 2020, "Soft Magnetic Tactile Skin for Continuous Force and Location Estimation Using Neural Networks," *IEEE Robot. Autom. Lett.*, **5**(3), pp. 1–1.
- [46] Ijaz, S., Li, H., Hoang, M. C., Kim, C.-S., Bang, D., Choi, E., and Park, J.-O., 2020, "Magnetically Actuated Miniature Walking Soft Robot Based on Chained Magnetic Microparticles-Embedded Elastomer," *Sens. Actuators A*, **301**, p. 111707.
- [47] Novelino, L. S., Ze, Q., Wu, S., Paulino, G. H., and Zhao, R., 2020, "Untethered Control of Functional Origami Microrobots With Distributed Actuation," *Proc. Natl. Acad. Sci. USA*, **117**(39), pp. 24096–24101.
- [48] Schaeffer, M., and Ruzzene, M., 2015, "Wave Propagation in Reconfigurable Magneto-Elastic Kagome Lattice Structures," *J. Appl. Phys.*, **117**(19), p. 194903.
- [49] Chen, T., Zhang, X., Yan, X., Zhang, B., Jiang, J., Huang, D., Qi, M., and Sun, R., 2019, "Harnessing Magnets to Design Tunable Architected Bistable Material," *Adv. Eng. Mater.*, **21**(3), pp. 1801255.
- [50] Guell Izard, A., and Valdevit, L., 2020, "Magnetoelastic Metamaterials for Energy Dissipation and Wave Filtering," *Adv. Eng. Mater.*, **22**(2), pp. 1901019.
- [51] Keten, S., Xu, Z., Ihle, B., and Buehler, M. J., 2010, "Nanoconfinement Controls Stiffness, Strength and Mechanical Toughness of β -Sheet Crystals in Silk," *Nat. Mater.*, **9**(4), pp. 359–367.
- [52] DeBenedictis, E. P., and Keten, S., 2019, "Mechanical Unfolding of Alpha- and Beta-Helical Protein Motifs," *Soft Matter*, **15**(6), pp. 1243–1252.
- [53] Fang, H., Chang, T.-S., and Wang, K. W., 2020, "Magneto-Origami Structures: Engineering Multi-Stability and Dynamics Via Magnetic-Elastic Coupling," *Smart Mater. Struct.*, **29**(1), p. 015026.
- [54] Livesley, R. K., 1975, *Matrix Methods of Structural Analysis*, Pergamon Press, Oxford.
- [55] Kidambi, N., and Wang, K. W., 2020, "Dynamics of Kresling Origami Deployment," *Phys. Rev. E*, **101**(6), pp. 063003–063003.
- [56] Lehner, G., 2010, *Electromagnetic Field Theory for Engineers and Physicists*, Springer, Berlin.
- [57] Furlani, E. P., 2001, *Permanent Magnet and Electromechanical Devices*, Academic Press, San Diego, CA.
- [58] Beleggia, M., Tandon, S., Zhu, Y., and De Graef, M., 2004, "On the Magnetostatic Interactions Between Nanoparticles of Arbitrary Shape," *J. Magn. Magn. Mater.*, **278**(1–2), pp. 270–284.
- [59] Vokoun, D., Beleggia, M., Heller, L., and Šittner, P., 2009, "Magnetostatic Interactions and Forces Between Cylindrical Permanent Magnets," *J. Magn. Magn. Mater.*, **321**(22), pp. 3758–3763.
- [60] Virtanen, P., Gommers, R., Oliphant, T. E., Haberland, M., Reddy, T., Cournapeau, D., Burovski, E., Peterson, P., Weckesser, W., Bright, J., van der Walt, S. J., Brett, M., Wilson, J., Jarrod Millman, K., Mayorov, N., Nelson, A. R. J., Jones, E., Kern, R., Larson, E., Carey, C. J., Polat, İ., Feng, Y., Moore, E. W., VanderPlas, J., Laxalde, D., Perktold, J., Cimrman, R., Henriksen, I., Quintero, E. A., Harris, C. R., Archibald, A. M., Ribeiro, A. H., Pedregosa, F., and van Mulbregt, P., and SciPy 1.0 Contributors, 2020, "SciPy 1.0: Fundamental Algorithms for Scientific Computing in Python," *Nat. Methods*, **17**(3), pp. 261–272.
- [61] Azulay, H., Lutaty, A., and Qvit, N., 2020, "Approach for Comparing Protein Structures and Origami Models," *Biochim. Biophys. Acta Biomembr.*, **1862**(2), pp. 183132–183132.
- [62] Hiromi, Y., Koshiro, Y., Yasuhiro, M., Richard, W., Raney Jordan, R., and Jinkyu, Y., 2020, "Data-Driven Prediction and Analysis of Chaotic Origami Dynamics," *Commun. Phys.*, **3**(1), pp. 1–8.
- [63] Kidambi, N., and Wang, K. W., 2019, "On the Deployment of Multistable Kresling Origami-Inspired Structures," *Proceedings of the ASME 2019 International Design Engineering Technical Conferences and Computers and Information in Engineering Conference, Volume 5B: 43rd Mechanisms and Robotics Conference, Anaheim, CA, Aug. 18–21, ASME, p. V05BT07A030.*

834 **Supplemental Information: Multi-stability Property of Magneto-**
 835 **Kresling Truss Structure**

836
 837 Xinyan Yang¹ , Sinan Keten^{1,2}

838 ¹ *Department of Civil & Environmental Engineering,*

839 *Northwestern University, 2145 Sheridan Road, Evanston, IL 60208, USA.*

840 ² *Department of Mechanical Engineering,*

841 *Northwestern University, 2145 Sheridan Road, Evanston, IL 60208, USA.*

842
 843 **NOTE 1. SELECTION OF PROPER MAGNETIC MOMENT MAGNITUDE TO CREATE**
 844 **TRI-STABLE STRUCTURES**

845 The number of stable states of a magneto-Kresling truss structure is determined by the initial height h_0 , radius
 846 R , initial rotation angle θ_0 , truss stiffness k , magnetic moment magnitude m and magnet arrangement. It is
 847 computationally expensive to study all $(h_0, R, \theta_0, k, m, \text{magnet arrangement})$ combinations. Therefore, we
 848 first fixed $R = 90$ mm, $k = 26.56$ N/m and took the magnet layout shown in Fig. 3 (c), then explored how the
 849 potential energy minima changes with increasing m^2 for several combinations of (h_0, θ_0) . Studied initial
 850 heights h_0 include 80 mm, 110 mm and 140 mm. Initial rotation angle θ_0 ranges from 0° to 100° at a spacing
 851 of 10° . Magnet strength m^2 increases from 0 to $2.0 \text{ A}^2 \cdot \text{m}^4$ linearly. The deformation domain (u, ϕ) was divided
 852 into five subdomains based on directions of the vertical displacement and rotation, i.e., four quadrants and
 853 the zone near the origin. The thresholds for u and ϕ to distinguish the origin zone and the other four quadrants
 854 were set such that the number of stable states detected in each subdomain is no more than one, in case the
 855 plot cannot show all of the local minima. We find for $n = 4$ and 6, the maximum number of stable states is
 856 two without any stable configuration falling in the high-energy contracted clockwise ($u < 0, \phi < 0$) or
 857 expanded anti-clockwise ($u > 0, \phi > 0$) quadrant. As n increases to 8, potential energy minima in the ($u < 0,$
 858 $\phi < 0$) quadrant were found. We notice minima in high-energy contracted clockwise quadrant (magenta block)
 859 and minima in low-energy contracted anti-clockwise quadrant (blue block) exchange their relative positions
 860 with respect to m^2 for $\theta_0 = 20^\circ$ and 30° at fixed height $h_0 = 110^\circ$ as illustrated in Supplemental Figure 1 (a)

861 and (b), respectively. We expect as θ_0 goes from 20° to 30° , the two blocks would appear at the same m^2 at
862 some point thus creating a tri-stable structure. This is validated in SupplementalMovie1. We finally set m^2 to
863 $0.785 \text{ A}^2 \cdot \text{m}^4$, which results in a tri-stable structure with initial configuration near $(h_0, \theta_0) = (110 \text{ mm}, 24^\circ)$.
864 Note the selection of m^2 is flexible, for example, we find other choices of m^2 can trigger tri-stability near $(h_0,$
865 $\theta_0) = (80 \text{ mm}, 24^\circ)$, as shown in Supplemental Figure 2. For $n = 10$, potential energy minima with a relatively
866 high strain energy are detected, but they do not co-exist with two additional minima. Thus, we do not observe
867 tri-stability for $n = 10$ in the limited combinations of (h_0, θ_0) we have studied.

868

869 **NOTE 2. MULTI-STABILITY DIAGRAMS OF MAGNETO-KRESLING TRUSS**
870 **STRUCTURES WITH A DIFFERENT ALTERNATE NODAL MAGNET**
871 **ARRANGEMENT BY FLIPPING TOP-LAYER DIPOLES**

872 Supplemental Figure 3 shows multi-stability diagrams of the magneto-Kresling truss structure with a
873 different alternate nodal magnet arrangement, where all top-layer magnetic dipoles in Fig. 3 (c) are flipped.
874 Magnets centered at node 1, 3, 5, 7, 9, 11, 13 and 15 have the same dipole moment along the $[0, 0, 1]$
875 direction, while at node 2, 4, 6, 8, 10, 12, 14 and 16, magnetic dipoles are along the $[0, 0, -1]$ direction.
876 For this layout, only mono-stable and bi-stable configurations are detected for $n = 4$ and 6, without any
877 unstable regions. An obvious shift of the initial geometry giving one or two stable states is observed
878 compared with the alternate arrangement discussed in the main text. We also find flipping the top-layer
879 magnets removes all tri-stable octagon-based ($n = 8$) magneto-Kresling truss structures but triggers the
880 tri-stability for $n = 10$ in the orange intersection zone between two yellow bands at large h_0 in
881 Supplemental Figure 3 (d). Considering the fact revealed in Fig. 9 that the original alternate arrangement
882 only creates tri-stable systems for $n = 8$, this interesting phenomenon provides us with the possibility of
883 exclusively developing the tri-stability in magneto-Kresling truss structures with a desired polygon shape
884 via varying nodal magnet arrangements.

885

886 **NOTE 3. MULTI-STABILITY DIAGRAMS OF MAGNETO-KRESLING TRUSS**
 887 **STRUCTURES WITH TOP AND BOTTOM MAGNETS ARRANGED IN A PURELY**
 888 **ATTRACTIVE PATTERN**

889 With $R = 90$ mm, $m^2 = 0.785$ A²·m⁴ and $k = 26.56$ N/m, multi-stability diagrams with nodal magnets all
 890 pointing upwards and thereby creating a pure attraction between the two plates are shown in Supplemental
 891 Figure 4. For $n = 4$, only mono-stable and bi-stable structures are found. Compared with the truss-only
 892 systems, the magnetostatic interaction changes the dependence of number of potential energy minima on
 893 initial configuration (h_0, θ_0) . As n increases from 6 to 10, unstable regions grow and the number of bi-stable
 894 structures diminishes. Also detected are some tri-stable structures near $\theta_0 = 0$. If nodal magnets are arranged
 895 in the attractive or repulsive pattern, magneto-Kresling truss structures with zero initial rotation angle are
 896 rotationally symmetric. Once a second stable state appears in the anti-clockwise folded shape, there must be
 897 a third one in the clockwise region with the same vertical displacement and energy. Thus, $\theta_0 = 0$ structures
 898 are always mono-stable or tri-stable.

899
 900 **NOTE 4. MULTI-STABILITY DIAGRAMS OF MAGNETO-KRESLING TRUSS**
 901 **STRUCTURES WITH TOP AND BOTTOM MAGNETS ARRANGED IN A PURELY**
 902 **REPULSIVE PATTERN**

903 If the magnetic dipoles on the bottom layer are all along $[0, 0, -1]$ direction, while top-layer ones are along
 904 $[0, 0, 1]$ direction, there would be a purely repulsive magnetic force between the two plates. Supplemental
 905 Figure 5 shows the multi-stability diagram for this case, again with $R = 90$ mm, $m^2 = 0.785$ A²·m⁴ and $k =$
 906 26.56 N/m. Unlike the attractive layout in NOTE 2, unstable structures only appear when $n = 4$ with purely
 907 repulsive interactions. For $n = 6, 8$ and 10 , two bi-stable bands (shade of yellow) in the figure intersect with
 908 each other and generate tri-stability (shade of orange) in the shared region extending from $\theta_0 = 0$ to higher θ_0
 909 configurations. The number of tri-stable cases increases with n . Examining Supplementary Figure 3, 4, 5 and
 910 Fig. 9 in the main text, it is evident that the purely repulsive arrangement of the magnets yields the broadest
 911 tri-stable region for each value of n , compared to purely attractive or alternating magnet arrangements.

912

913 **NOTE 5. DAMPED FREE VIBRATION TESTS OF A TRI-STABLE MAGNETO-**
 914 **KRESLING TRUSS STRUCTURE**

915 To show states $S0(0.00011h_0, 0.073^\circ)$, $S1(-0.68h_0, 50.78^\circ)$, and $S2(-0.79h_0, -124.49^\circ)$ we detected for the
 916 magneto-Kresling truss structure with $(h_0, \theta_0) = (107.80 \text{ mm}, 29.66^\circ)$ in section 3.2.2 are stable states the
 917 structure can rest at under a small perturbation when there is no external force applied, we performed
 918 numerical integrations using the Fourth Order Runge-Kutta method to simulate the dynamic response after
 919 releasing the structure at a position very close to the stable state with zero initial velocity. The equations of
 920 motion for this 2-DOF system are,

$$m\ddot{u} + c_u\dot{u} + F_z(u, \phi) = F_{penalty} \quad (\text{A1})$$

$$I\ddot{\phi} + c_\phi\dot{\phi} + T_z(u, \phi) = 0 \quad (\text{A2})$$

921 where m is the mass of the top plate, $m = 120 \text{ g}$. I is its moment of inertia, $I = mR^2$. $F_z(u, \phi)$ and $T_z(u, \phi)$ are
 922 the total resistance force along z -axis and torque about z -axis of the system undergoing deformation (u, ϕ) at
 923 time t , respectively, which were defined in section 2.2. Damping coefficient c_u was set to 1.85 N/(m/s) such
 924 that the damping ratio for the first mode (calculated at $S0$) is 0.4 . c_ϕ was set to $c_u \cdot R^2$. We selected a large
 925 damping ratio for the purpose of obtaining a stable system in a short period of time. To bound the response
 926 in the domain of our interest, we introduced a penalty function $F_{penalty}$ to the RHS of Eqn. (A1) and assumed
 927 perfect elastic collision at steric barrier $u = -0.8h_0$. The penalty function has the form,

$$928 \quad F_{penalty} = \begin{cases} -k_p(u + 0.8h_0), & u \leq -0.8h_0 \\ 0, & u > -0.8h_0 \end{cases}$$

929 This penalty function can be considered as a soft repulsion between the two plates, modeled by a one-sided
 930 harmonic potential with stiffness $k_p = 5 \text{ kN/m}$. The structure was released at 10 mm above and 5° (anti-
 931 clockwise) away from each stable state. The displacement time histories and the trajectories of the dynamic
 932 responses are shown in the left and right panels of Supplemental Figure 6, respectively. The time step was
 933 0.001s . In 5-s time integration, all systems ended up in the target states.

934

935 **NOTE 6. LINEAR CONFORMATIONAL CHANGE PATHWAY FOR A SPECIFIC**
 936 **OCTAGON-BASED MAGNETO-KRESLING TRUSS STRUCTURE TO REALIZE**
 937 **ENERGY STORAGE**

938 With $n = 8$, $R = 90$ mm, $m^2 = 0.785$ A²·m⁴, $k = 26.56$ N/m and alternate magnet layout in Fig. 3 (c), we find
 939 the structure with initial configuration $(h_0, \theta_0) = (86.47$ mm, $50.75^\circ)$ has the maximum normalized energy
 940 storage capacity of $\Delta E_{\max} = 2.25$. Supplemental Figure 7 depicts a pathway from the stable state S0 $(u, \phi) =$
 941 $(-0.077h_0, 5.67^\circ)$ near the origin to the second stable state S1 $(-0.76h_0, -141.60^\circ)$ with relatively high potential
 942 energy on its axial force, torque and energy landscape using white dashed lines. It is the shortest path
 943 generated from linear interpolation between the two states. With prescribed axial force and torque applied to
 944 the top polygon, the structure overcomes an energy barrier of height 4.53 then reaches S1 with 2.25
 945 normalized energy locked at that state as shown in Supplemental Figure 8. SupplementalMovie4 is the
 946 animation of this quasi-static loading process with transient input axial force and torque marked on the left.
 947 We define the energy density as the energy change normalized by the volume change of the magneto-Kresling
 948 truss cylinder when it switches from the first to the second stable state. Thus,

949
$$\text{Energy density} = \frac{\Delta \text{Energy}}{\Delta \text{Volume}} = \frac{2.25 \times k \times h_0^2}{\pi R^2 \times (h_{s1} - h_{s0})} = 0.297 \text{ J/L.}$$

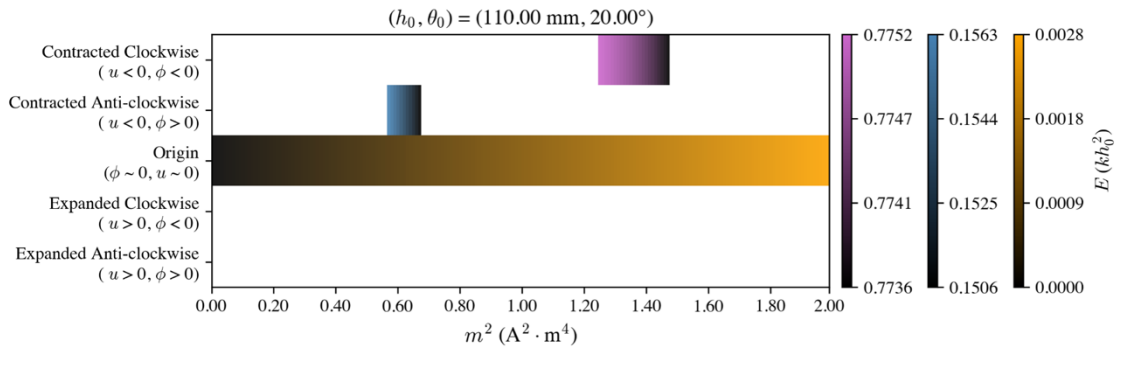
950

951

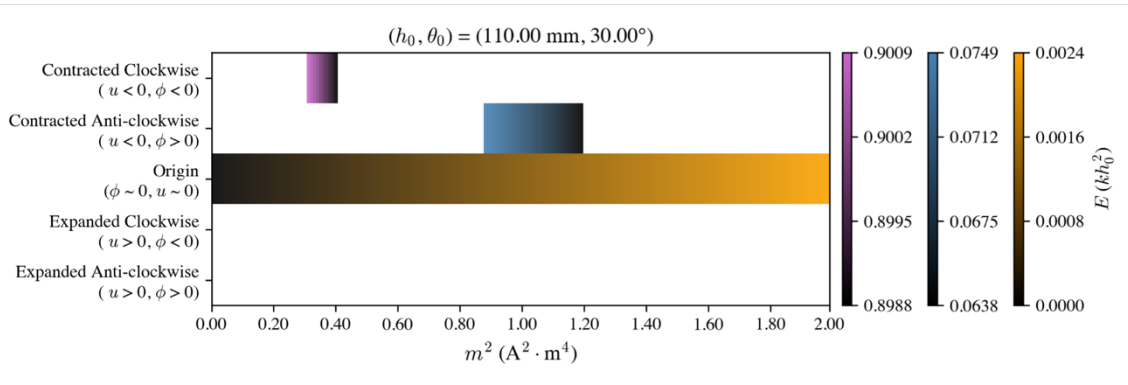
952

953 **SUPPLEMENTAL FIGURES**

954



(a)



(b)

955

956 **Supplemental Figure 1: Changes in the number and region of stable states with increasing magnetic strength m^2**

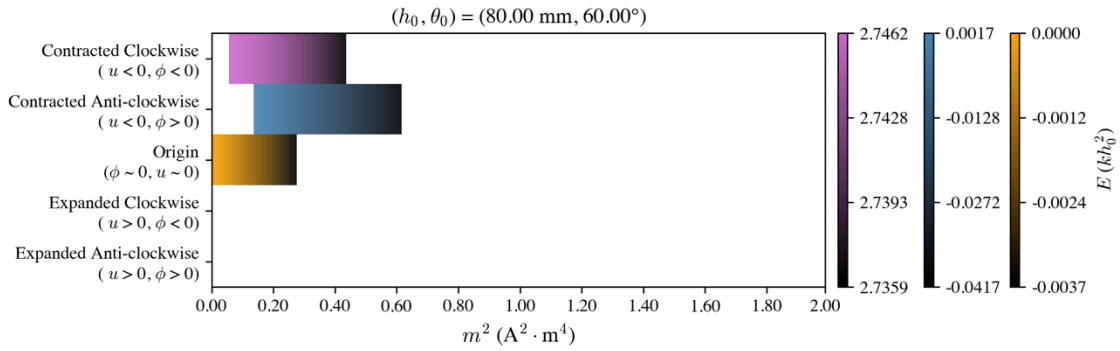
957 **for an octagon-based ($n = 8$) magneto-Kresling truss structure with (a) $(h_0, \theta_0) = (110 \text{ mm}, 20^\circ)$ and (b) $(h_0, \theta_0) =$**

958 **$(110 \text{ mm}, 30^\circ)$. Colors show the normalized total potential energy at each stable state. $n = 8, R = 90 \text{ mm}, k = 26.56$**

959 **N/m and nodal magnets take opposite dipole moment directions as shown in Fig. 3 (c).**

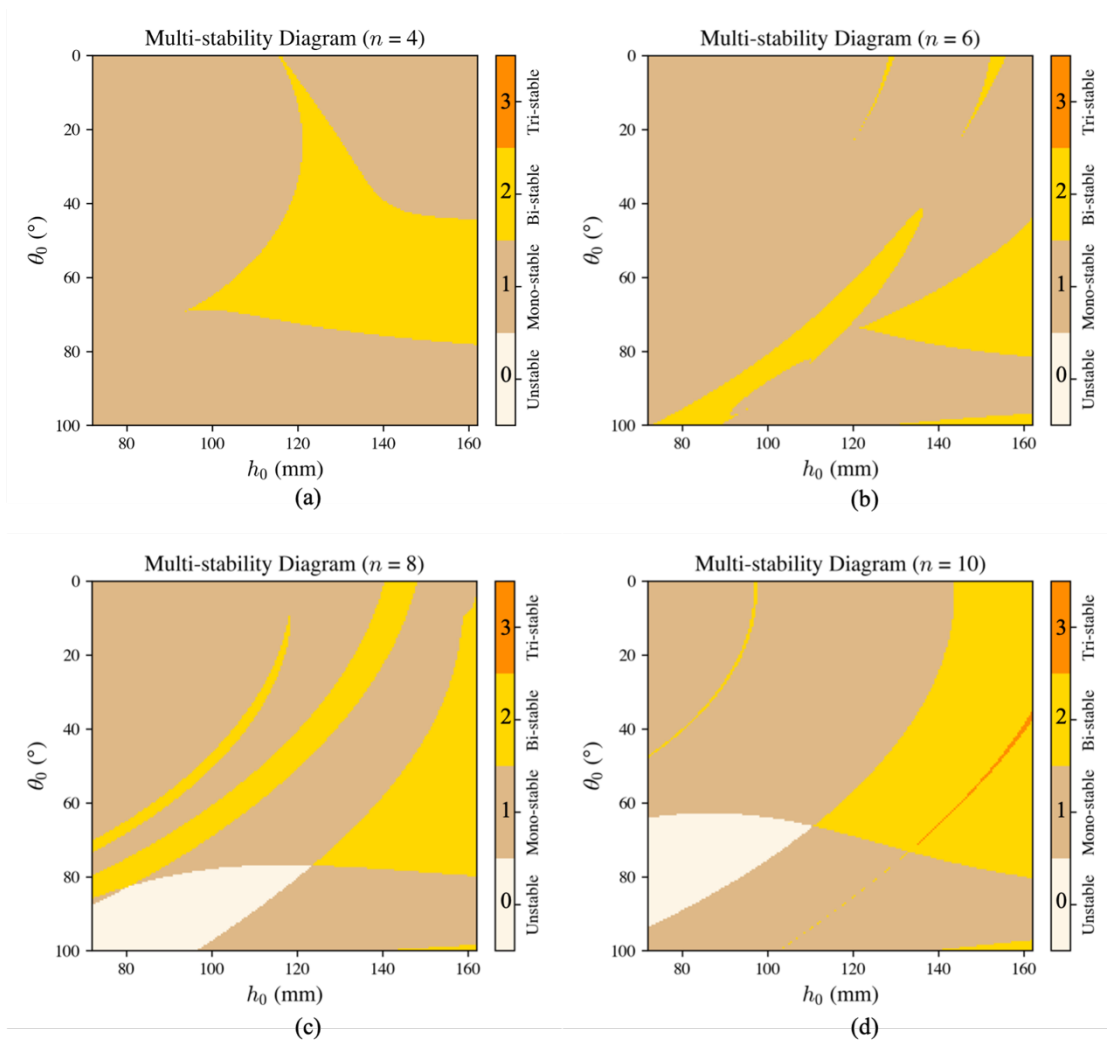
960

961



962

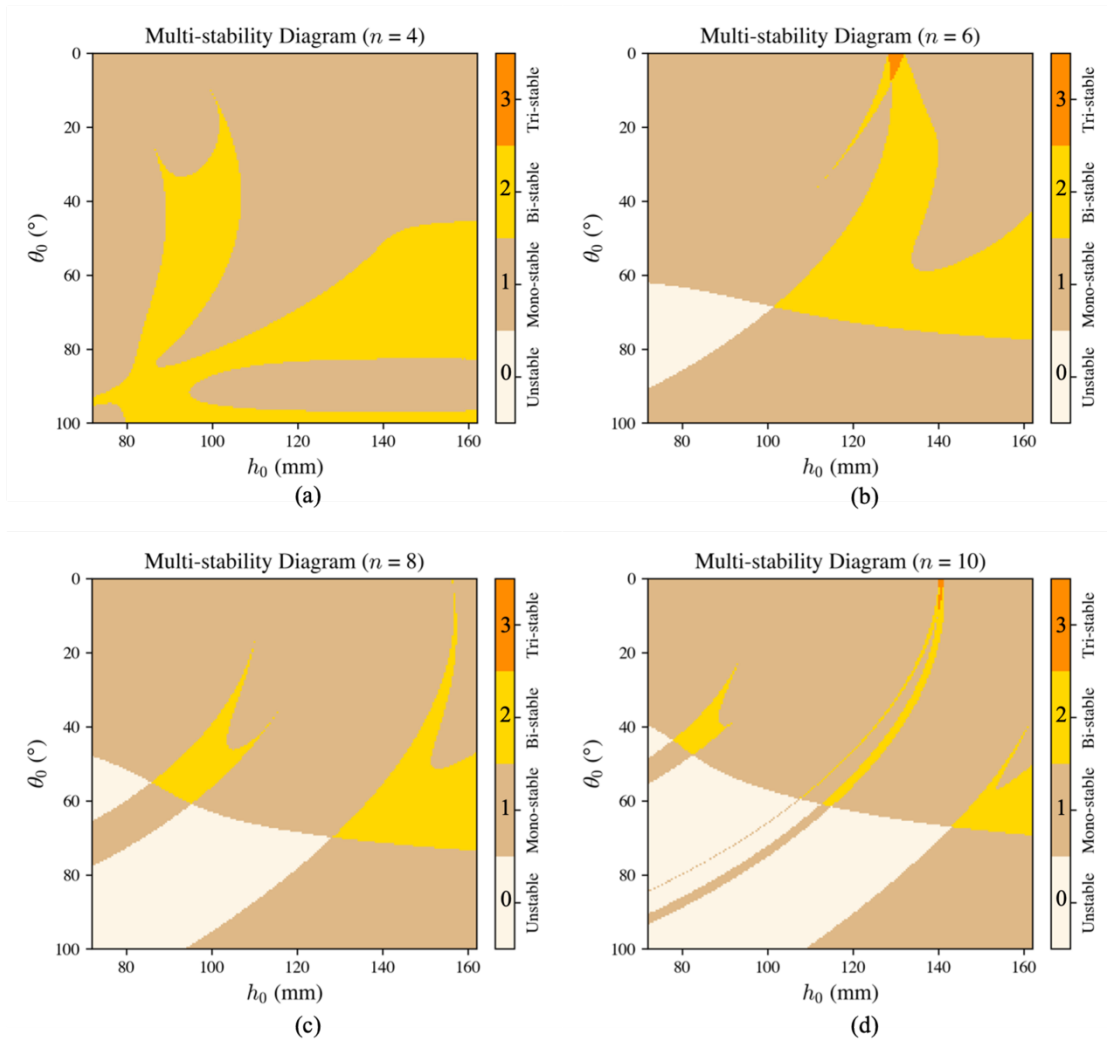
963 **Supplemental Figure 2: Changes in the number and region of stable states with increasing magnetic strength m^2**
 964 **for an octagon-based ($n = 8$) magneto-Kresling truss structure with $(h_0, \theta_0) = (80 \text{ mm}, 60^\circ)$. Colors show the**
 965 **normalized total potential energy at each stable state. $n = 8, R = 90 \text{ mm}, k = 26.56 \text{ N/m}$ and nodal magnets take**
 966 **opposite dipole moment directions as shown in Fig. 3 (c).**



967

968 **Supplemental Figure 3: Multi-stability diagrams showing the number of stable states found numerically for**
 969 **magneto-Kresling truss structures with different initial configurations (h_0, θ_0) in the domain of interest ($u \geq -0.8h_0,$**
 970 **$\phi_{\min} \leq \phi \leq \phi_{\max}$). Unstable, mono-stable, bi-stable and tri-stable regions illustrate cases with zero, one, two and**
 971 **three stable states, respectively. Diagrams are made for (a) $n = 4$, (b) $n = 6$, (c) $n = 8$ and (d) $n = 10$ with $R = 90$**
 972 **$\text{mm}, m^2 = 0.785 \text{ A}^2 \cdot \text{m}^4$ and $k = 26.56 \text{ N/m}$. Nodal magnets take an alternate arrangement with all magnetic dipoles**
 973 **in the top layer in Fig. 3 (c) flipped.**

974



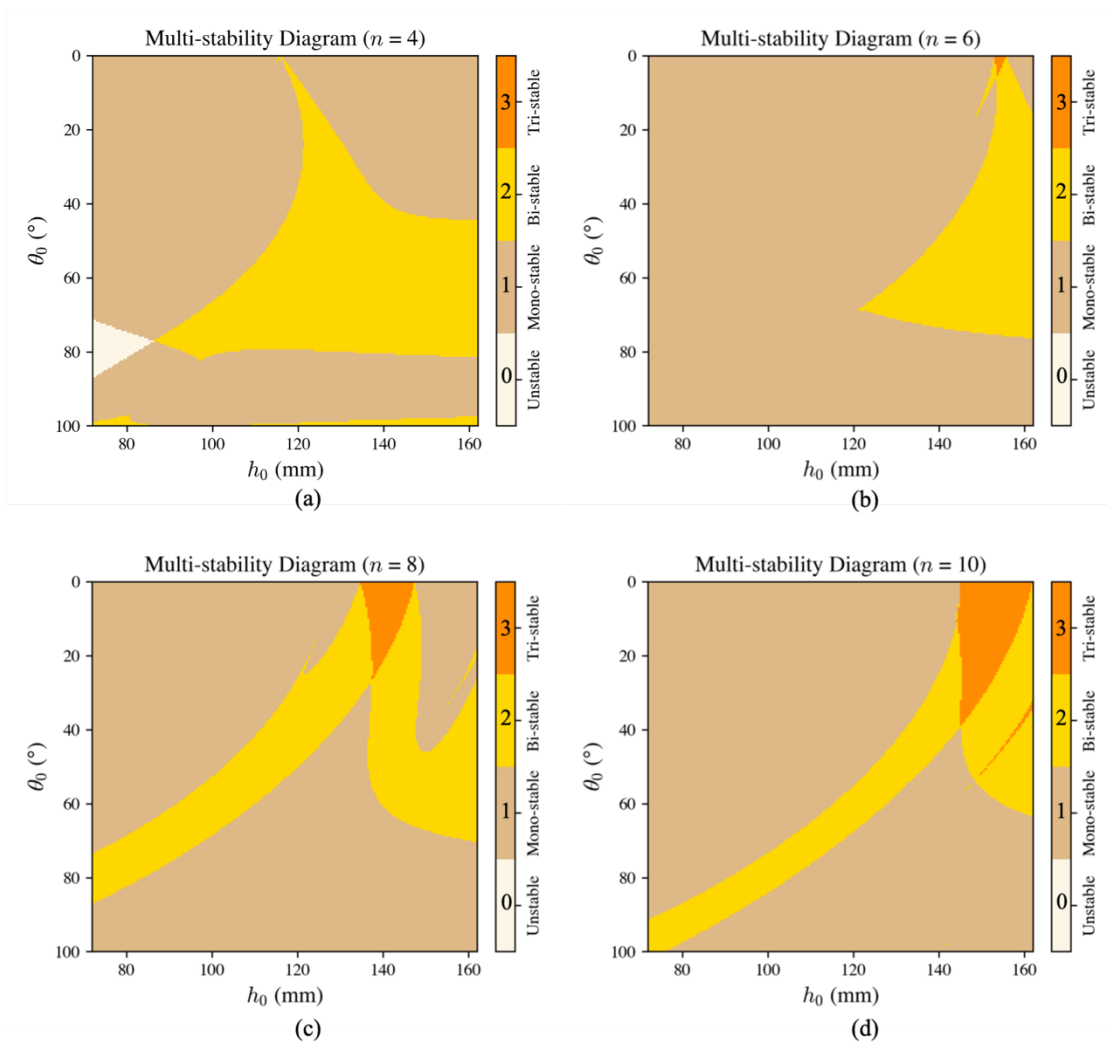
975

976 **Supplemental Figure 4: Multi-stability diagrams showing the number of stable states found numerically for**
 977 **magneto-Kresling truss structures with different initial configurations (h_0, θ_0) in the domain of interest $(u \geq -0.8h_0,$**
 978 **$\phi_{\min} \leq \phi \leq \phi_{\max})$. Unstable, mono-stable, bi-stable and tri-stable regions illustrate cases with zero, one, two and**
 979 **three stable states, respectively. Diagrams are made for (a) $n = 4$, (b) $n = 6$, (c) $n = 8$ and (d) $n = 10$ with $R = 90$**
 980 **mm , $m^2 = 0.785 \text{ A}^2 \cdot \text{m}^4$ and $k = 26.56 \text{ N/m}$. Nodal magnets take the attractive arrangement, i.e., all magnets point**
 981 **upwards.**

982

983

984



985

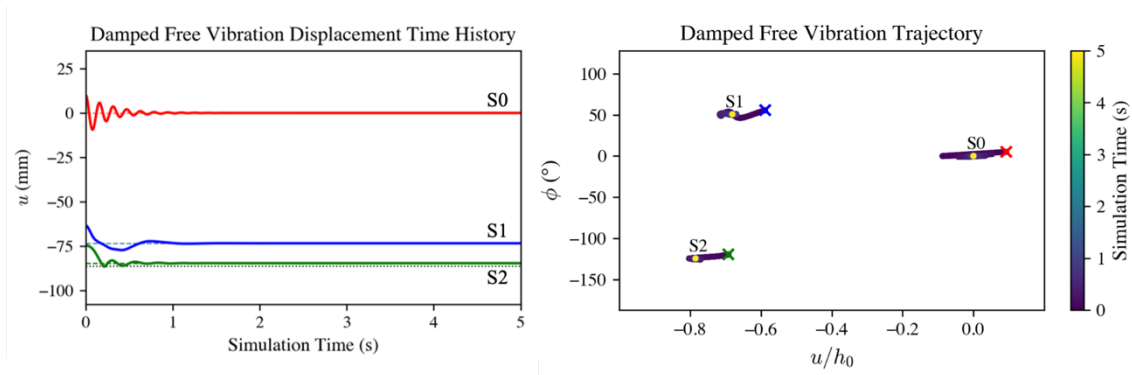
986 **Supplemental Figure 5: Multi-stability diagrams showing the number of stable states found numerically for**
 987 **magneto-Kresling truss structures with different initial configurations (h_0, θ_0) in the domain of interest ($u \geq -0.8h_0$,**
 988 **$\phi_{\min} \leq \phi \leq \phi_{\max}$). Unstable, mono-stable, bi-stable and tri-stable regions illustrate cases with zero, one, two and**
 989 **three stable states, respectively. Diagrams are made for (a) $n = 4$, (b) $n = 6$, (c) $n = 8$ and (d) $n = 10$ with $R = 90$**
 990 **mm, $m^2 = 0.785 \text{ A}^2 \cdot \text{m}^4$ and $k = 26.56 \text{ N/m}$. Nodal magnets take the repulsive arrangement, i.e., magnets on the top**
 991 **layer and bottom layer point upwards and downwards, respectively.**

992

993

994

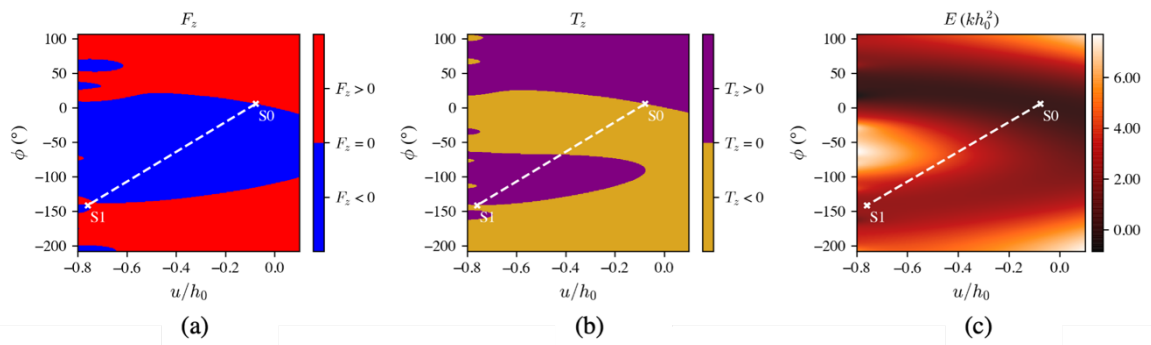
995



996 **Supplemental Figure 6: Left: Displacement time histories of the system released from 10 mm above and 5° (anti-**
 997 **clockwise) away from stable state S0, S1 and S2 are shown with solid lines in red, blue and green, respectively.**
 998 **The dashed lines with the same colors show the corresponding stable state positions. The black dotted line marks**
 999 **the position of assumed steric barrier at $u = -0.8h_0$. Right: Trajectories of the three damped systems undergoing**
 1000 **free vibration in the (u, ϕ) space. Color evolves with simulation time. Crosses with the same color scheme as the**
 1001 **left panel show the starting positions for the three trajectories.**

1002

1003



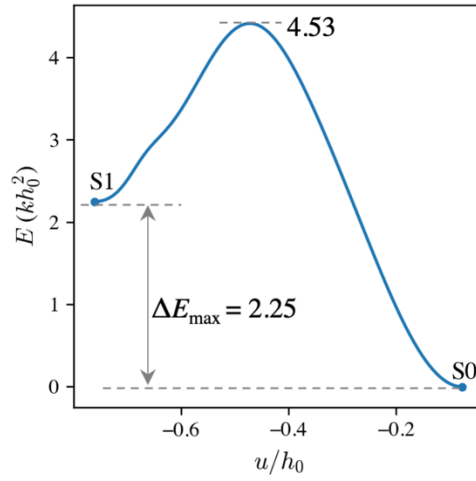
1004

1005 **Supplemental Figure 7: (a) Force F_z , (b) torque T_z applied on the top polygon, (c) normalized total potential energy**
 1006 **E in (u, ϕ) space for the octagon-based bi-stable magneto-Kresling truss structure with initial configuration $(h_0,$**
 1007 **$\theta_0) = (86.47 \text{ mm}, 50.75^\circ)$. The dashed white line depicts the transition path from stable state S0 to S1 by linear**
 1008 **interpolation. Only the sign of the force and torque is shown in panel (a) and (b) to highlight locations with zero**
 1009 **force and zero torque, respectively. Stable states are marked by white crosses. $R = 90 \text{ mm}$, $k = 26.56 \text{ N/m}$ and m^2**
 1010 **$= 0.785 \text{ A}^2 \cdot \text{m}^4$. Nodal magnets take opposite dipole moment directions as shown in Fig. 3 (c).**

1011

1012

1013



1014 **Supplemental Figure 8: Change of the normalized potential energy with the vertical displacement in the switch**
1015 **from S0 to S1 along the linear path shown in Supplemental Figure 7.**